International Journal of Multiphase Flow 36 (2010) 533–548

Contents lists available at ScienceDirect

International Journal of Multiphase Flow

journal homepage: www.elsevier.com/locate/ijmulflow

# Measurement accuracy of a mono-fiber optical probe in a bubbly flow

Jiří Vejražka [a,*], Marek Večeř [a,b], Sandra Orvalho [a], Philippe Sechet [c], Marek C. Ruzicka [a], Alain Cartellier [c]

[a] Institute of Chemical Process Fundamentals, Czech Academy of Sciences, Rozvojova 135, 16502 Prague, Czech Republic
[b] VSB-Technical University of Ostrava, 17. listopadu, 70833 Ostrava – Poruba, Czech Republic
[c] Laboratoire des Ecoulements Géophysiques et Industriels (CNRS/UJF/Grenoble-INP), BP 53, 38041 Grenoble, France

ARTICLE INFO

*Article history:*
Received 4 August 2009
Received in revised form 25 January 2010
Accepted 13 March 2010
Available online 1 April 2010

*Keywords:*
Optical probe
Bubble–fiber interaction
Void fraction
Measurement error
Chord distribution

ABSTRACT

The measurement accuracy of a mono-fiber optical probe is studied experimentally using isolated bubbles rising freely in a still liquid. The dwell time of the probe tip within the gas phase, which is obtained from both the optical probe signal and high-speed visualization, is compared with the value expected for a non-perturbed bubble. The difference originates mainly from the intrusive nature of the optical probe, which modifies the bubble behavior when it comes into contact with the probe tip. This interaction increases the dwell time if the bubble is pierced by the probe near its pole, and shortens it for piercing near the equator. The mean dwell time, obtained by averaging for various piercing locations, is shortened and the local void fraction indicated by the probe is thus underestimated. It is shown that the void fraction error can be correlated with a modified Weber number, and this correlation is helpful for sensor selection and for uncertainty estimate. In addition, the distribution of gas dwell time usually differs from the response expected for an ideal probe. This deviation results from the dependence of the dwell time error on the piercing location. The dwell time distribution can be used to infer the dependence of the dwell time on the piercing location. Finally, the deformation of long fibers during the bubble-probe interaction significantly increases the measurement error. Observed results are consistent with data of Andreotti (2009), which were measured in an airlift flow, suggesting that present results are applicable also to the case of moving liquid. Conclusions of this study could be applied also to conductivity probes or more generally to the interaction of a bubble with any kind of thin, intrusive sensor or fiber.



## 1. Introduction

Two-phase gas–liquid systems are widely encountered in industrial applications, as either gas bubbles in liquids or liquid drops in gases. The two-phase mixtures are usually non-transparent and the usual flow-investigation methods (e.g. visual observation, PIV or LDA) are of limited help. Therefore, probes based on heat transfer or temperature changes, conductivity probes, back light scattering probes, RTG tomography, X- or γ-ray adsorption, or wire-mesh sensors are employed for characterization of such mixtures. For review of these methods, see Tropea et al. (2007) or Grimes et al. (2006).

One of the most common tools for multiphase flow studies is the optical probe. It is an intrusive instrument, which was first described by Miller and Mitchie (1970). It is based on measuring the light reflection from a tip of an optical fiber, which is placed in the measuring point in a gas–liquid mixture. The typical arrangement of the measuring system is shown in Fig. 1. The sensitive probe tip is fabricated by shaping a standard glass fiber used in telecommunications (Cartellier, 1998; Cartellier and Barrau, 1998a; Saito and Mudde, 2001). The other end of the fiber is split in two branches. One is connected to a light source (e.g. a laser diode) and the other leads the reflected light to a photodetector, which generates an analog output signal. Because of the difference in the refractive indices of liquid and gas phases, the amount of reflected light depends on the phase surrounding the tip. The photodetector output voltage has either high or low level if the probe tip is located in gas or liquid, respectively. Bubbles moving over the probe tip thus generate a signal that consists of a succession of low and high level parts (Fig. 1). This signal is useful for the determination of the local void fraction. Single as well as multiple probes can also be used for the estimation of bubble velocity (Cartellier, 1992; Cartellier and Barrau, 1998a,b; Guet et al., 2003), Sauter mean size (Revankar and Ishii, 1992, 1993), bubble size distribution, interfacial area density or number density flux (Cartellier 1999).

One can define a phase-indicator function $\psi(t)$ that is $\psi(t) = 0$ if a point of interest point is occupied by liquid at time $t$, and that rises to $\psi(t) = 1$ if there is gas (bubble) there. The dwell time $\tau_i$ of $i$th bubble is the time, during which the point of interest lays inside

* Corresponding author. Tel.: +420 220 390 250.
*E-mail addresses:* jiri@vejrazka.net (J. Vejražka), marek.vecer@vsb.cz (M. Večeř), orvalho@icpf.cas.cz (S. Orvalho), sechet@hmg.inpg.fr (P. Sechet), ruzicka@icpf.cas.cz (M.C. Ruzicka), cartellier@hmg.inpg.fr (A. Cartellier).

0301-9322/$ - see front matter © 2010 Elsevier Ltd. All rights reserved.
doi:10.1016/j.ijmultiphaseflow.2010.03.007

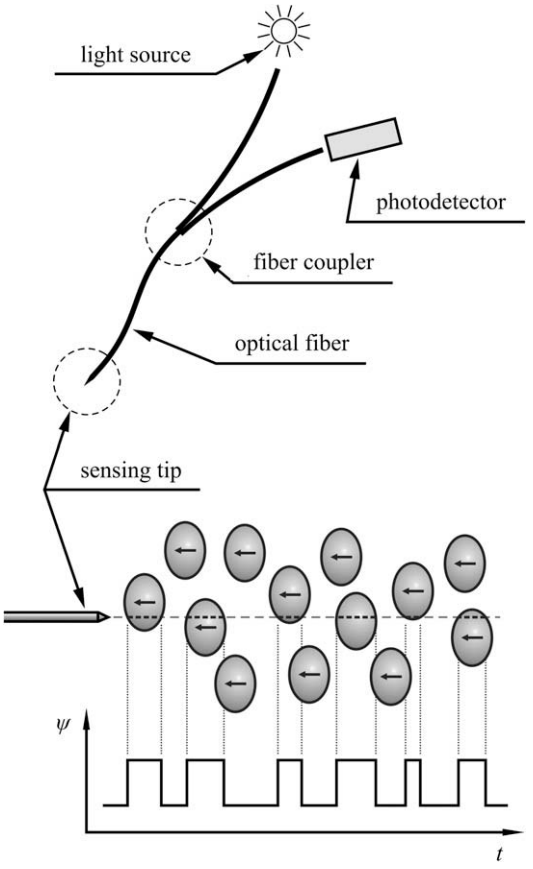


**Fig. 1.** A scheme of the optical probe measurements.

this bubble, i.e. during which the phase-indicator function remains $\psi = 1$. The set of dwell times $\tau_i$ can be further analyzed. The mean dwell time $\overline{\tau}$ and the probability density function (p.d.f.) of the dwell time, $p_\tau(\tau)$, are usually calculated. The local void fraction $\alpha$ is then determined as

$$\alpha = \lim_{t_{tot}\to\infty} \frac{\sum \tau_i}{t_{tot}} = \lim_{t_{tot}\to\infty} \frac{N\overline{\tau}}{t_{tot}}, \tag{1}$$

where $t_{tot}$ is the total time during that $\psi(t)$ is studied and $N$ is the number of bubbles passing through the point of interest. Often, results are interpreted in terms of the chord length, i.e. the dwell time multiplied by the bubble velocity. The mean dwell time is used to evaluate the mean chord length, and the dwell time p.d.f. provides information about the chord length distribution. The bubble size distribution can be calculated on basis of these data (see Cartellier (1999) for detailed discussion).

To obtain $\psi(t)$ experimentally by an optical probe, its tip is introduced into the point of interest and the output signal is reduced to a phase-indicator function, $\psi_{op}(t)$. It is then processed in an analogous way to $\psi(t)$: the dwell times $\tau_{op,i}$ are extracted from $\psi_{op}(t)$, the local void fraction $\alpha_{op}$ is calculated analogously to (1) and the dwell time p.d.f. $p_{\tau,op}(\tau)$ is evaluated. The experimental evaluation of $\psi(t)$ suffers, however, from a weakness consisting in the intrusive nature of the optical probe. The interaction of the probe with the bubbles modifies the bubble motion and shape. At the same time, the bubbles can deform the tiny probe tip and move its sensitive part from the point of interest. Due to both effects, the optical probe output $\psi_{op}(t)$ does not exactly match the phase-indicator function $\psi(t)$ in a fixed point in an unperturbed flow, but it indicates the phase presence in a moving point in a flow, which is obstructed by the probe. Consequently, the experimentally measured void fraction $\alpha_{op}$ and the p.d.f. of dwell time $p_{\tau,op}(\tau)$ differ from their ideal counterparts $\alpha$ and $p_\tau(\tau)$. The difference between $\psi(t)$ and $\psi_{op}(t)$, caused by the mutual interaction between the bubbles and the probe, is the principal source of error of the measurements.

Several studies have addressed the measuring uncertainty of optical probes. Barrau et al. (1999) integrated the void fraction profiles, which were measured by the optical probe in upward co-current bubbly flows, and compared the resulting gas hold-up with the value obtained using the fast-closing valve technique. For air–water flows with bubble size above 1 mm and absolute bubble velocities between 10 and 100 cm/s, the optical probe underestimated the gas hold-up by 1–15%. Barrau et al. have also tried to identify the mechanisms yielding to these errors and they suggested three most important phenomena: (i) blinding, referring to an error due to local bubble deformation near the probe tip, (ii) crawling, which is caused by a bubble deformation at bubble-size scale and/or by a change of its velocity during the contact, and (iii) drifting, which is caused by the modification of the liquid velocity field and consequent changes in the bubble trajectory.

Kiambi et al. (2003) measured the dwell time by a double-tip optical probe and independently by using a high-speed camera. They compared the probability density functions of both dwell times. In air–water system, the optical probe was found to underestimate the dwell time. The error of its mean was 12% and 6% for 2.15 and 4.5 mm bubbles, respectively, moving with velocities comprised between 30 to 40 cm/s. The same error could be expected for the void fraction measurements with similar bubbles. The dwell time p.d.f. shifted to shorter dwell times.

Juliá et al. (2005) (available also in Harteveld, 2005) carefully performed a similar experiment with a mono-fiber stretched optical probe. They studied the effect of bubble-to-probe offset (distance $x$ depicted in Fig. 2) on the bubble piercing process and on the error of the dwell time. When piercing the bubble near its pole ($x/a_x$ smaller than about 0.5, see Fig. 2 for meaning of $a_x$), the dwell time was overestimated due to bubble deceleration, whilst it was underestimated because of a significant bubble deformation when piercing near the equator. Juliá et al. (2005) also integrated the dwell time profiles to get the bubble volume. The probe underestimated it by 6.5%, 3.7% and 2.8% for air-in-water bubbles with sizes of 2.8, 3.7 and 5.2 mm, respectively. The absolute bubble velocities were in range 22–28 cm/s.

Chaumat et al. (2007) analyzed measurements made by a double-tip optical probe in conditions of an industrial-scale bubble column, with either an air–water or air-cyclohexane system. Bubble velocity was of order of 0.5–2 m/s and the bubble Sauter mean size was in range from 4 to 10 mm. They found, beside others, a significant underestimation of the measured gas hold-up, which exceeded 30% in some cases.

Finally, the p.d.f. of the dwell time for 30 and 140 μm optical probe was provided by Cartellier and Rivière (2001) for an almost mono-dispersed bubbly flow with spherical bubbles (see Fig. 7 of this reference). For both probes, $p_\tau(\tau)$ seriously differs from an ideal dwell time distribution. While the ideal p.d.f. is monotonically increasing with $\tau$, the observed p.d.f. is oppositely decreasing

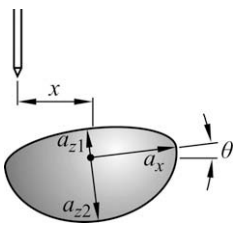


**Fig. 2.** Considered bubble geometry.

with $\tau$, especially in the case of the larger probe. This deviation is quite common but it has never been satisfactorily explained.

In this study, we will focus on differences between $\psi(t)$ and $\psi_{op}(t)$ and their consequences on the accuracy of the determination of the local void fraction and of the dwell time p.d.f. One of our objectives is to determine, how the void fraction error depends on the bubble size and on the bubble approach velocity. Another objective is to provide an insight into the phenomena responsible for the difference between the ideal and experimentally observed dwell time p.d.f.'s. In our experiments, we have used a mono-fiber optical probe with a conical tip. Our approach is similar to that of Juliá et al. (2005): we study an interaction of the optical probe with isolated bubbles rising in a still liquid. The bubble dwell time $\tau_{op}$, obtained from the optical probe signal, is compared with an estimate of $\tau$ obtained from the high-speed imaging. This comparison is repeated for various bubble-probe offsets (distance $x$ in Fig. 2). The mean dwell time $\overline{\tau_{op}}$ is calculated, compared with $\overline{\tau}$ and the expected error on the void fraction measurements is evaluated. The dependence of the measurement error on the bubble size is studied. To test how the error depends on the bubble velocity, we have also studied the bubble-probe interaction in liquids with higher viscosities (glycerin solutions). Similarly, by assuming the random offset $x$, the dwell time p.d.f. $p_{\tau,op}(\tau)$ is estimated and compared with $p_\tau(\tau)$.

For applicability of our results on accuracy of void fraction measurements to different systems, the bubble-probe interaction is characterized by suitable dimensionless numbers. The error, caused by the probe intrusive nature, is their function. Three dimensionless parameters are needed: two for the characterization of the rising bubble and another one for describing the probe diameter. The set of dimensionless numbers suitable for describing bubble-probe interaction consists of $M$, $Ca$ and $We$. The first of them is the modified Weber number, $M = \rho D^2 u_1{}^2/(\sigma D_{op})$, where $D$ is the bubble volume-equivalent size, $D_{op}$ is the diameter of probe fiber, $u_1$ is the bubble velocity before coming into contact with the probe, $\rho$ is the liquid density and $\sigma$ is the liquid surface tension. $M$ characterizes the ability of a bubble to overcome the surface-tension forces coming from the probe tip. It is a ratio of bubble momentum ($\sim \rho D^3 \cdot u_1$) to the impulsion of the surface-tension force from the probe ($\sim \sigma D_{op} \cdot D/u_1$). The second dimensionless number is the capillary number, $Ca = \mu u_1/\sigma$, where $\mu$ is the liquid viscosity. It describes the relative importance of viscosity and surface-tension effects and it also is the controlling parameter for the thickness of the film being deposited on the probe tip (see e.g. Quéré, 1999). Finally, the last parameter is the Weber number, $We = \rho \varpi D u_1{}^2/\sigma$, which compares the inertial and surface-tension effects at the bubble-size scale. In the case of small bubbles in low-viscosity liquids, $We$ determines the bubble shape. With the above definitions, it holds $M = We\ D/D_{op}$. We also remark that the rising bubble itself is described here by $Ca$ and $We$ instead of a more common choice of the Morton and Eötvös numbers, $Mo = g\mu^4/(\rho\sigma^3)$, $Eö = \rho g D^2/\sigma$; however, if the bubble moves at the terminal conditions, $Ca$ and $We$ are uniquely related to these two numbers, at least in clean systems (Clift et al., 1978).

In this paper, we will show that the measurement error of the local void fraction caused by the probe intrusive nature can be correlated with $M$ and eventually a kind of correction can be applied. We will see that probes with a long tip might noticeably deform during the interaction, increasing greatly the measuring error. We will demonstrate that the probe intrusive nature causes an important deviation of $p_{\tau,op}(\tau)$ from $p_\tau(\tau)$. The $p_{\tau,op}(\tau)$ data, obtained on basis of our experiments in stagnant liquid, will be compared with that obtained by Andreotti (2009) in his airlift experiment, in which the liquid flows. The agreement will suggest that conclusions of this work are (to some extent) applicable also to the case of moving liquid. Finally, it will be demonstrated that the importance of probe's intrusive nature can be evaluated also on the basis of $p_{\tau,op}(\tau)$ data, if these are obtained in a mono-dispersed and uniform bubbly flow.

## 2. Description of experiments

### 2.1. Experimental setup

The experimental setup used in this study is depicted in Fig. 3. The bubble-probe interaction was studied in a rectangular glass vessel with a square bottom of inner size 11 × 11 cm and height of 26 cm. A bubble generator was placed in the vessel bottom. The bubble generator is a device that produces bubbles of prescribed size by imposing their detachment by a rapid needle motion (Vejrazka et al., 2008). The optical probe was inserted into the vessel from the top. It was the "Type 1C Probe" delivered by A2 Photonic Sensors Ltd., Grenoble, France. The probe consists of a metallic body (1.5 mm in diameter), from whose end the optical fiber protrudes by 15 mm. The fiber diameter was $D_{op} = 0.13$ mm and its tip, produced by etching process, has an apex angle of 30°. The probe was fixed to a 2D traversing device, by which its position was adjusted in the horizontal plane. The probe tip was located typically 2 cm above the tip of bubble generator's needle.

The interaction of the optical probe tip with a bubble rising in a stagnant liquid was recorded by a high-speed camera (Redlake HS-4), at frame rate ranging from 3500 to 15,000 fps (typically 10,000

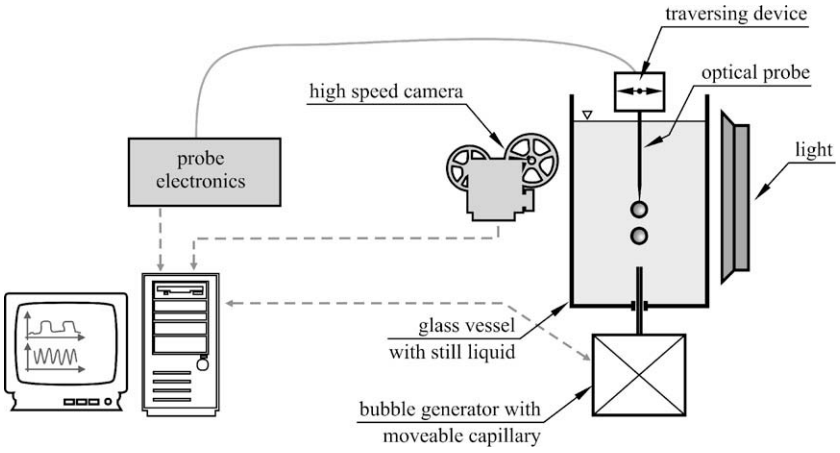


**Fig. 3.** The schema of experimental setup.

**Table 1**
Physical properties of used liquids.

| Liquid | wt. concentration (%) | $T$ (°C) | $\rho$ (kg m$^{-3}$) | $\mu$ (MPa s) | $\sigma$ (mN m$^{-1}$) | $Mo$ (−) |
|---|---|---|---|---|---|---|
| Water | – | 30.1 | 995.6 | 0.797 | 71.2 | $1.10 \times 10^{-11}$ |
| Glycerin 8 | 60 | 25.9 | 1152.0 | 8.87 | 65.3 | $1.89 \times 10^{-7}$ |
| Glycerin 20 | 70 | 27.1 | 1174.2 | 13.6 | 60.5 | $1.29 \times 10^{-6}$ |

fps), with resolution of at least 170 × 512 pixels. The camera was fit with Nikon AF Nikkor 50 mm f/1.8D lens, which was mounted using extension rings of length ranging from 20 to 48 mm. The lens was mounted reversely with help of a reversion ring (i.e. the objective was oriented with its frontal lens toward the camera body). The optical magnification was ranging from 0.8 to 1.23, the camera pixel pitch was 12 μm and the resulting image scale was thus ranging from 9.6 to 14.8 μm/pixel. The bubble-probe interaction was observed in diffuse backlight. The illumination system consisted of a 500 W halogen lamp and two diffusers (opaque glass plates, not shown in Fig. 3). In front of the lamp, there was a 10 cm thick glass vessel (also not shown in Fig. 3) filled with water to protect the experimental vessel from lamp's heat.

A computer instrumented with a multifunction data acquisition board (National Instruments PCI-6221) recorded the output signal from the optical probe and also the camera synchronization signal. The acquisition rate was 125 kHz for each channel. A care was taken about proper synchronization of the probe signal recording and the high-speed imaging.

### 2.2. Experimental conditions, procedures and data processing

The experiments were performed with air bubbles in water and in two glycerin solutions. The water was distilled and additionally filtered by a set of ionic resin filters and an activated carbon filter. The glycerin solutions were prepared using water of the same quality and pure p.a. grade glycerin. See Table 1 for physical properties of the liquids. The air was dried and filtered with a particle and activated carbon filters.

When experimenting, a bubble was produced by the bubble generator, the optical probe signal was recorded and the high-speed movie of the bubble-probe interaction was acquired synchronously. The high-speed images were then treated using single-purpose software, which was written in Matlab® and which used the Image Processing Toolbox. The treatment consisted of two major steps: (A) Image processing, during which the points laying at the bubble boundary were detected, and (B) boundary fitting, during which the detected boundary was fitted with a smooth curve, and the bubble size and position of its center-of-mass was found for this smoothed boundary.

The step (A) consisted of following sub-steps: (i) A background image was subtracted from each treated frame. (ii) The frames were transformed to binary images by comparing pixel values to a threshold. (iii) Isolated small objects, appearing due to image noise, were removed. (iv) Boundary pixels of the resulting object (bubble) were detected in each frame. (v) These boundary curves were smoothed for each frame. The smoothing procedure was visually checked to preserve the bubble shape with good accuracy. This smoothed boundary was stored for each frame and it was used for constructing the phase-indicator functions $\psi_g$ and $\psi_{ref}$, which will be described in Section 2.3.

For the step (B), a *double-ellipse curve* (curve consisting of two halves of an ellipse, with the same semimajor axis $a_x$, but different semiminor axes $a_{z1}$ and $a_{z2}$, and inclined by $\theta$, Fig. 2) was found as the best fit of smoothed bubble boundaries. This fitted boundary was then used for inferring the following parameters for each image frame (Fig. 2): the semimajor axis $a_x$, semiminor axes $a_{z1}$ and $a_{z2}$, the aspect ratio $\chi = 2a_x/(a_{z1} + a_{z2})$ and the inclination angle $\theta$. The center-of-mass coordinates $x_b$ and $z_b$ and the bubble volume-equivalent diameter $D$ were calculated, assuming bubble axial symmetry. The bubble velocity was calculated by differentiating the center-of-mass position. Finally, the bubble-probe offset $x$ (Fig. 2) was found as a difference between $x_b$ and the horizontal probe position in the last frame before contact.

When experimenting, the bubble generator was adjusted to produce bubbles of a given size. The offset $y$ (same as $x$, but in the direction parallel with the camera axis) was carefully set to zero. To do so, the probe was moved both in $+y$ and $-y$ direction to positions, when the bubbles just touch the probe, and then the probe was placed in the middle of these two positions. The probe was then moved step-by-step to positions with different bubble-probe offsets $x$. This scanning across the bubble was repeated for

**Table 2**
Operating conditions of present experiments.

| Liquid | $D$ (mm) | $u_1$ (cm/s) | $\chi$ (−) | $C$ (−) | $We$ (−) | $Re$ (−) | $Ca$ (−) | $Eö$ (−) | $M$ (−) | $C\,M\,\chi^{2/3}$ (−) |
|---|---|---|---|---|---|---|---|---|---|---|
| Water | 0.69 | 18.1 | 1.05 | 0.527 | 0.32 | 156 | $2.03 \times 10^{-3}$ | 0.065 | 1.68 | 0.91 |
| Water | 0.89 | 25.3 | 1.12 | 0.571 | 0.79 | 280 | $2.83 \times 10^{-3}$ | 0.107 | 5.39 | 3.32 |
| Water | 1.12 | 30.6 | 1.26 | 0.657 | 1.47 | 428 | $3.43 \times 10^{-3}$ | 0.172 | 12.6 | 9.66 |
| Water | 1.48 | 35.9 | 1.62 | 0.878 | 2.67 | 663 | $4.02 \times 10^{-3}$ | 0.300 | 30.3 | 36.7 |
| Water | 1.78 | 36.6 | 1.97 | 1.098 | 3.34 | 816 | $4.10 \times 10^{-3}$ | 0.436 | 45.9 | 79.2 |
| Water | 2.23 | 33.6 | 2.45 | 1.399 | 3.52 | 937 | $3.76 \times 10^{-3}$ | 0.683 | 60.5 | 154 |
| Glycerin 8 | 1.16 | 11.2 | 1.02 | 0.511 | 0.26 | 16.9 | $1.52 \times 10^{-2}$ | 0.234 | 2.30 | 1.19 |
| Glycerin 8 | 1.45 | 8.4 | 1.05 | 0.528 | 0.18 | 15.8 | $1.14 \times 10^{-2}$ | 0.363 | 2.01 | 1.09 |
| Glycerin 8 | 1.50 | 13.8 | 1.06 | 0.535 | 0.50 | 26.9 | $1.87 \times 10^{-2}$ | 0.389 | 5.81 | 3.23 |
| Glycerin 8 | 2.18 | 21.2 | 1.18 | 0.611 | 1.73 | 60.0 | $2.88 \times 10^{-2}$ | 0.822 | 29.0 | 19.8 |
| Glycerin 8 | 3.01 | 26.0 | 1.51 | 0.810 | 3.59 | 102 | $3.53 \times 10^{-2}$ | 1.57 | 83.0 | 88.4 |
| Glycerin 20 | 1.26 | 10.3 | 1.02 | 0.509 | 0.26 | 11.2 | $2.31 \times 10^{-2}$ | 0.301 | 2.50 | 1.29 |
| Glycerin 20 | 1.39 | 11.1 | 1.02 | 0.512 | 0.33 | 13.4 | $2.49 \times 10^{-2}$ | 0.368 | 3.56 | 1.85 |
| Glycerin 20 | 1.52 | 11.5 | 1.03 | 0.517 | 0.39 | 15.1 | $2.58 \times 10^{-2}$ | 0.437 | 4.54 | 2.39 |
| Glycerin 20 | 1.84 | 17.8 | 1.06 | 0.534 | 1.13 | 28.3 | $3.99 \times 10^{-2}$ | 0.642 | 16.0 | 8.85 |
| Glycerin 20 | 2.31 | 19.9 | 1.13 | 0.579 | 1.77 | 39.7 | $4.46 \times 10^{-2}$ | 1.01 | 31.5 | 19.8 |
| Glycerin 20 | 2.80 | 21.8 | 1.27 | 0.661 | 2.58 | 52.8 | $4.89 \times 10^{-2}$ | 1.49 | 55.6 | 43.0 |
| Glycerin 20 | 3.03 | 22.4 | 1.34 | 0.709 | 2.95 | 58.7 | $5.02 \times 10^{-2}$ | 1.75 | 68.7 | 59.3 |

several bubble sizes in each liquid. The bubble size ranged from 0.7 to 3 mm and the corresponding characteristics of bubbles (equivalent diameter $D$, first-contact velocity $u_1$, aspect ratio $\chi = 2a_x/(a_{z1} + a_{z2})$, added-mass coefficient $C$, and dimensionless numbers $We$, $Re = \rho u_1 D/\mu$, $Ca$, $Eö$ and $M$) are presented in Table 2. The added-mass coefficient $C$ was calculated from the bubble aspect ratio following Lamb (1932, §114) as:

$$C = \frac{\Lambda(\chi)}{2 - \Lambda(\chi)}, \tag{2}$$

where

$$\Lambda(\chi) = \int_0^\infty \frac{d\lambda}{(\lambda + \chi^{-4/3})^{3/2}(\lambda + \chi^{2/3})} \tag{3}$$

and $\lambda$ is an integration parameter.

The bubbles were rising vertically and their inclination $\theta$ was negligible at the time they hit the probe. Their shape was steady, with exception of the largest bubble in water, which was slightly wobbling ($a_{z1}$ and $a_{z2}$ were evolving during the bubble rise, while $a_x$ and $a_{z1} + a_{z2}$ remained almost constant). The bubbles hit the probe with velocity $u_1$ close to its terminal-rise value. Fig. 4a compares the bubble velocity (at the time of first contact with the probe) to the Moore's (1965) prediction for terminal rise, and Fig. 4b compares the aspect ratio $\chi$ with the same prediction. In the case of water, Moore (1965) over-predicts $\chi$ for larger bubble sizes. This is a known weakness of the Moore's estimate (Duineveld 1995), which leads also to a slight under-prediction of the rise velocity for larger bubble sizes (it is also visible in Fig. 4a). The agreement for the rise velocity is, however, generally good and this suggests that the bubble interface was not contaminated and was mobile. In the case of glycerin solutions, the observed rise velocities are higher than the prediction. This is caused by an inappropriateness of Moore's model for the case of relatively low Reynolds number (Blanco and Magnaudet 1995). Surfactant presence is difficult to avoid in glycerol solutions and it might be responsible for a certain scatter of experimental data.

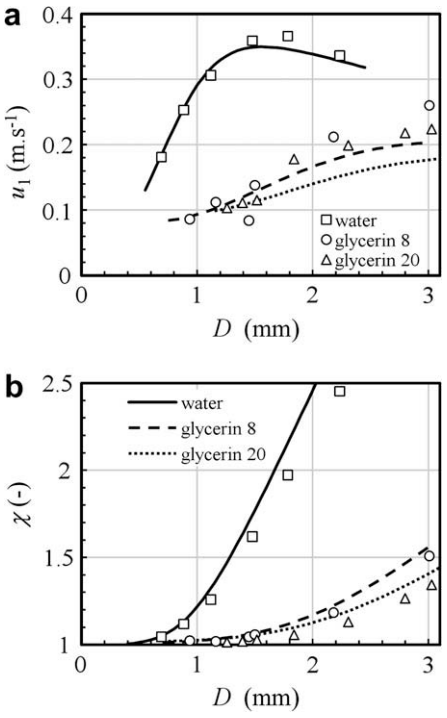


**Fig. 4.** Comparison of experimentally observed: (a) bubble rise velocity and (b) bubble aspect ratio with prediction of Moore (1965).

The estimations of the experimental errors are provided: The image processing itself is very precise owing to good quality of acquired high-speed movies. The boundary points are within ±1 pixel from the real boundary and the same estimates hold for the error of the bubble size (the bubble size was typically larger than 100 pixels). The error of the bubble velocity is below 2% before the first contact of the bubble with the probe. In the case of the bubble that is in contact with the probe, the velocity error considerably increases because the double-ellipse fit is no more suitable for fitting the bubble shape. Consequently, the evaluation of center-of-mass position is less accurate. We believe that the velocity error is still lower than 5% of the initial velocity in these cases. In the case of non-zero bubble-probe offset $x$, the bubble moreover losses its axial symmetry and it is principally not possible to fully reconstruct its three-dimensional shape (hence also center-of-mass position and velocity); evaluation of error is difficult in this case. Finally, the accurate setting of $y$ offset to zero is essential for proper interpretation of present experiments, because the bubble projection observed by the camera is meaningful only in this case. The real offset in $y$ direction was within ±0.02 mm from zero; this value corresponds to a play of the traversing device.

### 2.3. Definition of phase-indicator functions

On basis of the experimental data, we construct three different phase-indicating functions $\psi(t)$. One of them ($\psi_{op}$) is based on the optical probe signal, while the two others ($\psi_g$ and $\psi_{ref}$) are created using the information provided by high-speed imaging. We remind that the instantaneous value of $\psi$ is zero if the probe tip is located in the liquid and it is unity if the tip is in gas. To construct the phase-indicator function, the time of bubble first contact with the probe tip $t_1$ and the time of last contact $t_2$, when $\psi(t)$ should switch, have to be determined. The dwell time of the measuring location within the bubble is found as $\tau = t_2 - t_1$.

The optical probe phase-indicating function $\psi_{op}$ is obtained from the photodetector voltage signal $S(t)$ by comparing it with a threshold value $\Delta S_{\min}$ (Fig. 5a), which was set slightly above the noise level of the "in liquid" signal. The time of first contact $t_{op1}$ is the instant when the threshold level is exceeded. Juliá et al. (2005) and Barrau et al. (1999) discuss two different criteria for the determination of the last-contact time $t_{op2}$: either (i) falling back below the threshold level or (ii) the instant of last signal maxima before this fall. We have used the latter criteria. Owing to the large signal slope, both $t_{op1}$ and $t_{op2}$ were insensitive to the threshold level $\Delta S_{\min}$ or to the choice of the last contact instant criteria. Note that Juliá et al. (2005) reported sensitivity to the last contact criteria, especially when the bubble touches the probe very near its equator. Smaller sensitivity in our case might be a consequence of a much sharper tip of etched probe used in this study.

Following Juliá et al. (2005), a phase-indicating function, denoted as $\psi_g$ in this paper, is constructed on basis of the high-speed imaging. For each image, the distance $d$ (Fig. 5b) between the probe tip and the nearest point of bubble boundary is measured. If the probe tip is inside the bubble, $d$ is considered negative. The first and the last-contact times $t_{g1}$ and $t_{g2}$ are found by interpolating for zero $d$. The images used for building $\psi_g$ are obtained during the bubble–probe interaction, when the bubble is perturbed by the contact with the probe. The phase-indicator function $\psi_g$ is therefore influenced by the probe intrusive nature. As it will be shown later, the optical fiber exposed to the flow is long enough to bend and hence the sensitive tip is laterally displaced during the interaction with the bubble. Because the distance $d$ is evaluated toward the initial position of the probe tip, $\psi_g$ is free of probe deformation effects. Yet, it includes the distortion of the bubble shape.

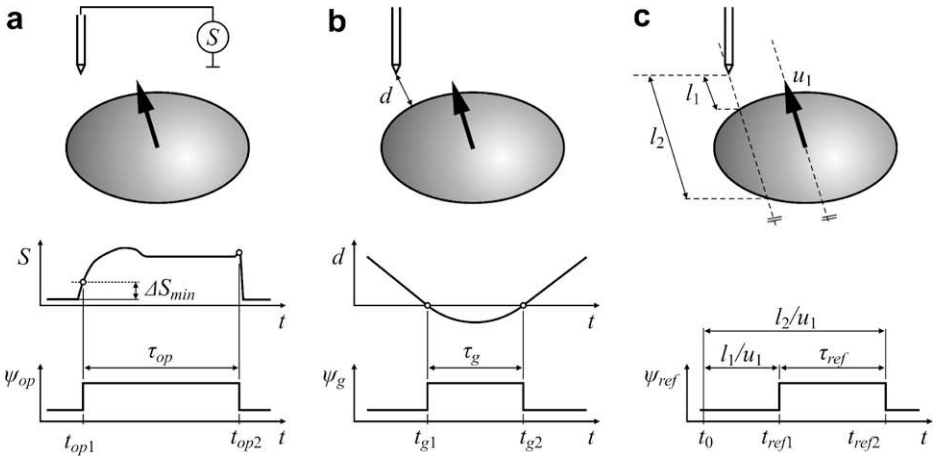


**Fig. 5.** Reconstruction of phase-indicator functions for: (a) optical probe, (b) rigid probe (based on high-speed imaging), (c) reference probe (based on high-speed imaging).

The high-speed imaging provides also a phase-indicating function $\psi_{ref}$, which is based only on images obtained before the first bubble contact with the probe. It is assumed that the approaching bubble maintains its initial shape, velocity and direction. The shape is determined from the last frame (taken at time $t_0$), in which the probe tip is still observed outside the bubble. The distances $l_1$ and $l_2$ (see Fig. 5c) are measured and the corresponding instants of the first and the last contact are calculated as $t_{ref1} = t_0 + l_1/u_1$ and $t_{ref2} = t_0 + l_2/u_1$, respectively. The phase-indicator function $\psi_{ref}$ is based only on a single image taken at time $t_0$ and on the bubble velocity before contact $u_1$; $\psi_{ref}$ is hence not affected by the probe intrusive nature. This phase-indicator function is meaningful only if bubbles are rising with a constant velocity before the first contact and if they are not changing their shape. Both these conditions were satisfied in the present study.

The following discussion on measurement accuracy of optical probes is based on a comparison of the three phase-indicator functions. The function $\psi_{op}$ issues from the *optical probe* signal, as described above. The function $\psi_g$, based on high-speed images, could be produced by an imaginary probe, which has the same intrusive character in terms of interface deformation and bubble trajectory modification as a real optical probe, but which does not deform; this imaginary probe will be thereinafter referred to as a *rigid probe*. Finally, $\psi_{ref}$ could be produced by another imaginary probe, which is free of intrusive character. We refer to this imaginary probe as *reference probe* and we will use its signal $\psi_{ref}$ for reference purposes when studying intrusiveness of the real optical probe.

## 3. Experimental results

### 3.1. High-speed imaging observations

The typical video records of the bubble-probe interaction are displayed in Fig. 6. No change of bubble velocity or shape was observed during its approach to the optical probe tip. This could be indeed expected as the probe tip is sharp and its diameter is small compared to the bubble size. To put this behavior in perspective, let us recall that in the case of cleaved probes with relatively large diameter compared to bubble size, strong deceleration occurs before contact (Wedin et al., 2003).

The bubble gets disturbed only after coming in contact with the optical probe tip. The large bubbles move more or less with their initial velocity (Fig. 6a and b). Their interface is deformed in the region that touches the probe. In the case of small bubble-probe offset, their upper part gets concave. Smaller bubbles are also deformed and their motion is more affected (Fig. 6c and d). In the case of small offset, bubble can stop or even move down during the contact and it is then deflected from its initial trajectory a while after (Fig. 6c). The deflection remains important in the case of non-zero bubble-probe offset (Fig. 6d). These changes of bubble shape and velocity are a consequence of probe's intrusive nature. Finally, a deformation of the optical probe is observed if the bubble is pierced near its equator. This is visible in Fig. 6b and d, where the initial probe position is shown by an arrow.

The bubble disturbance from the probe is further documented in Fig. 7, where the initial and terminal bubble shapes are compared. The background photos were taken at time $t_{ref2}$, when the bubble would have the last contact with the reference probe (which is non-intrusive). The dotted contours show the shape and position of the non-disturbed bubble at this time, i.e. it is the bubble contour at time $t_0$ just shifted by distance $l_2$ (Fig. 5c) in direction of bubble motion. This dotted contour would overlap with the observed bubble shape if the bubble is not affected by the probe. This is not the case, as bubble changes its velocity and shape during its interaction with the probe.

In agreement with Juliá et al. (2005), two different bubble behaviors are observed in dependence of bubble-probe offset $x$. In the case of small $x$ (first column in Fig. 7), the bubble is decelerated during the interaction. This is apparent from the bubble position, which is lower than the expected position of non-disturbed bubble. As a result of this deceleration, the probe tip is still located inside the bubble at ideal last-contact time $t_{ref2}$. The deceleration is hence delaying the last-contact time $t_{op2}$ indicated by the probe, compared to $t_{ref2}$.

In the case of larger $x$ (third and fourth columns in Fig. 7), the vertical bubble position corresponds roughly to an expected position for non-perturbed bubble, or it is even higher. This shows that the bubble can oppositely accelerate when piercing near the equator. A significant bubble deformation is observed in the part of interface, which is touching the probe. Due to this horizontal shrinking, the probe tip is already located outside the bubble at time $t_{ref2}$. This suggests that the bubble deformation advances the last-contact time $t_{op2}$, indicated by the probe, when compared to $t_{ref2}$.

The last-contact time indicated by the probe, $t_{op2}$, is hence delayed in the case of piercing at small $x$ (near the pole), and it is oppositely advanced when piercing at large $x$ (near the equator). These two effects are attributed to bubble deceleration and deformation, respectively, and they counteract. For a specific offset, they cancel each other, and the optical probe indicates the ideal last-

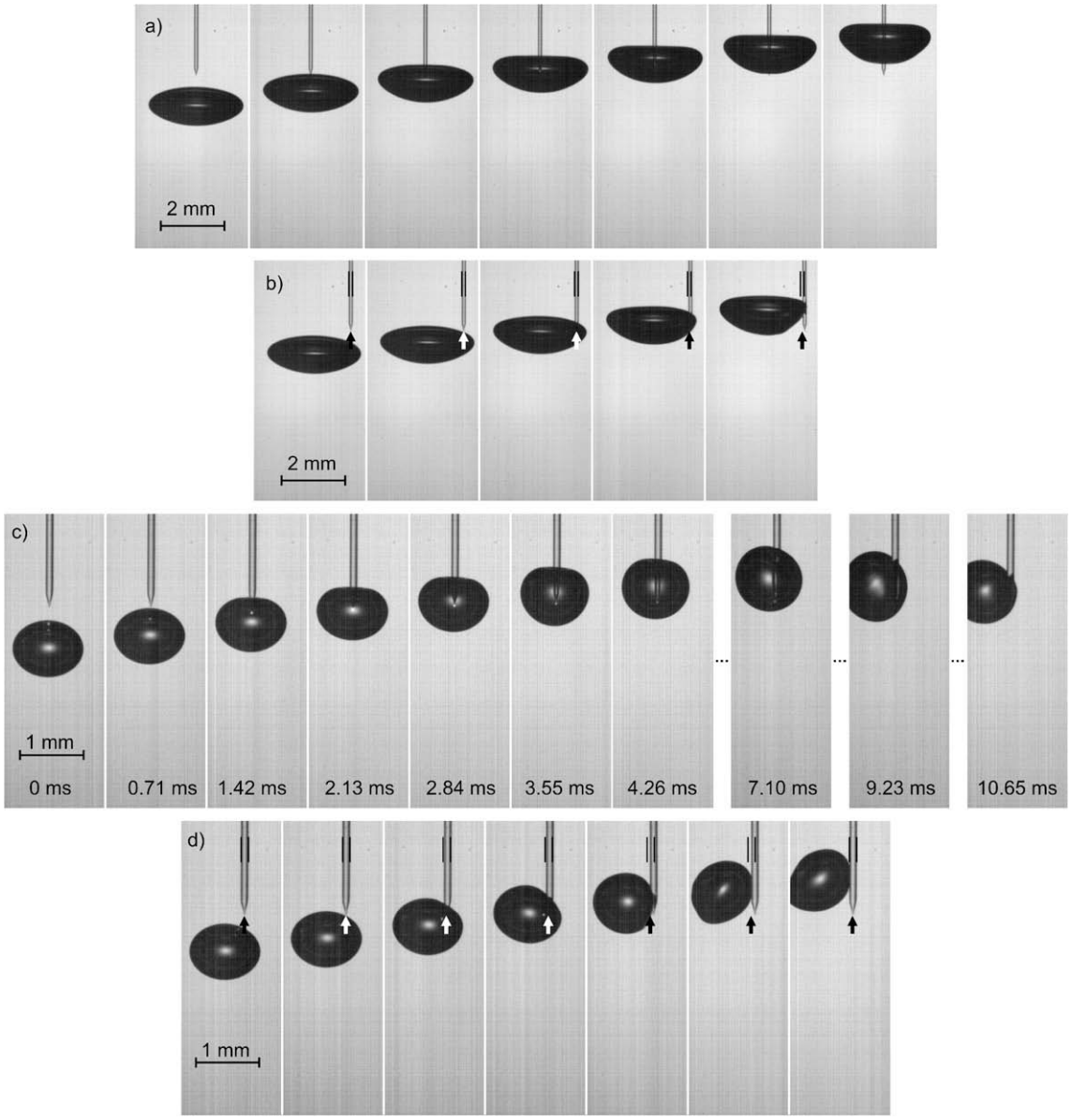


**Fig. 6.** High-speed records of the bubble-probe interaction in water. The bubble size and the frame interval are (a) and (b) $D = 2.23$ mm, 997 μs; (c) and (d) $D = 1.12$ mm, 710 μs. In (c), some frames are omitted. Arrows and lines in (b) and (d) indicate the initial position of the optical probe to show its deformation.

contact time, $t_{op2} = t_{ref2}$. Corresponding terminal bubble shapes are shown in the second column of Fig. 7. It is seen from these figures that even at this offset, at which the probe indicates correct last-contact time, the bubble is perturbed by the interaction with the optical probe.

### 3.2. Probe signal and phase-indicating functions

The typical time series $S(t)$ of optical probe output is shown in Fig. 8 for three bubble-probe offsets. Differences in the duration of the "gas level" part of signal are the only noticeable changes when the offset $x$ is modified (compare Figs. 8a and b). The signal approaches to a "bell shaped" signal described by Cartellier (1992) and Juliá et al. (2005), when the probe hits a very border of the bubble (Fig. 8c). The falling edge of such signal is less steep. This effect is, however, of lower importance here than observed by Juliá et al. (2005), possibly because of a sharper probe tip.

The three phase-indicating functions deduced from either the optical probe signal ($\psi_{op}$) or high-speed imaging ($\psi_g$, $\psi_{ref}$) are also compared in Fig. 8. The first contact time of the three phase-indicator functions is almost the same. This demonstrates the negligible effect of the probe on bubble behavior before the first contact and it is consistent with observation and analysis of the local interface deformation during piercing (Liju et al., 2001). Oppositely, the three last-contact times significantly differ. Previously discussed effects of delaying $t_{op2}$ relative to $t_{ref2}$ in the case of small $x$ (Fig. 8a) and of its advancing for large $x$ (Figs. 8b and c) are reflected. We will hence concentrate on the shift of the last-contact time.

The comparison of $\psi_{op}$ and $\psi_g$ is quite revealing. For most bubble-probe offsets (Fig. 8a), they are very similar and their minor difference can be attributed to the experimental uncertainty (error on time information in $\psi_g$ is related to the time interval between movie frames, which was about 0.1 ms). The similar character of $\psi_{op}$ and $\psi_g$ is expected, as both indicate if the probe tip is inside or outside the bubble. Only when the probe touches the bubble near its equator (Fig. 8b and c), an important difference between $\psi_{op}$ and $\psi_g$ appears. Both functions give the same result on the first

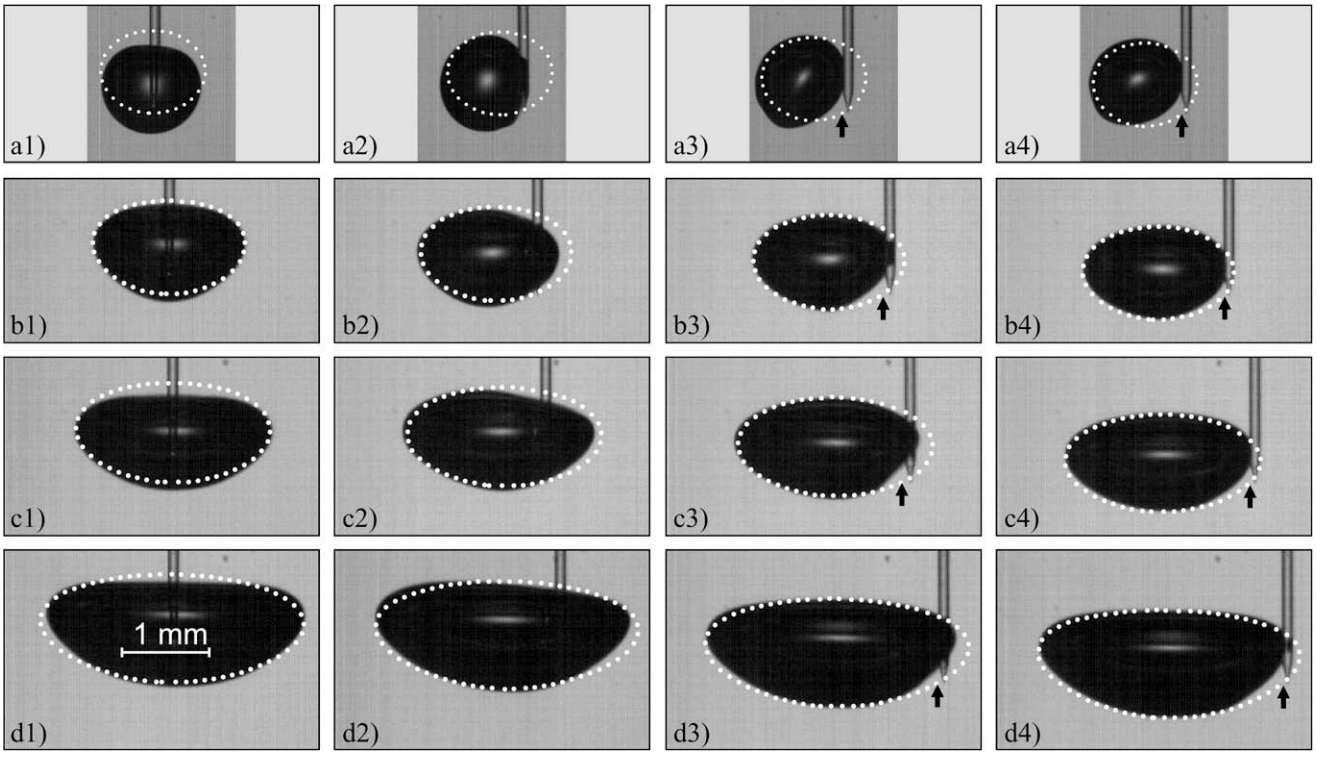


**Fig. 7.** Comparison of the initial and the terminal bubble shape. Snapshots are taken at time $t_{ref2}$. White dotted lines show the bubble contour at time $t_0$, which was displaced by distance $l_2$ in direction of velocity vector $u_1$ (see Fig. 5c). Arrows indicate the position of the probe tip before the first contact with the bubble. Time sequence for cases d1, d3, a1 and a3 is shown in Fig. 6. Observations in water, bubble sizes are 1.12, 1.48, 1.78 and 2.23 mm (from the top).

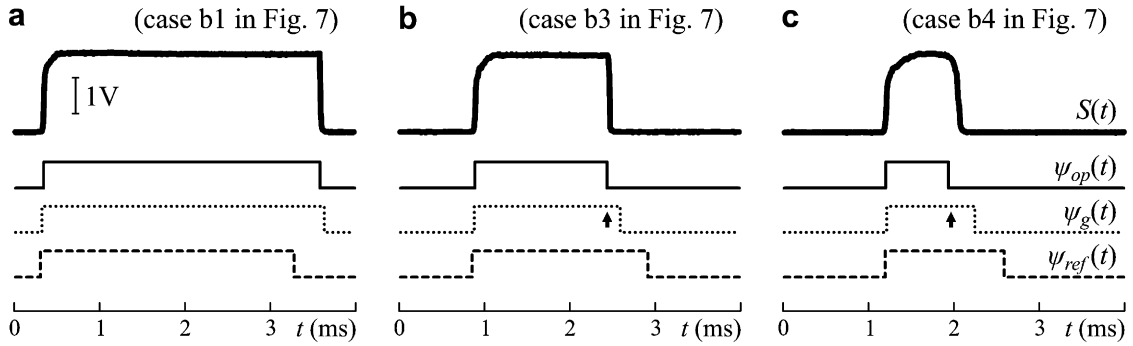


**Fig. 8.** Optical probe signal $S(t)$, and phase-indicating functions $\psi_{op}(t)$, $\psi_g(t)$ and $\psi_{ref}(t)$ for three cases shown in Fig. 7. Arrows show the falling time of $\psi_g$ (i.e. last contact $t_{g2}$), if it is evaluated with respect to final probe position.

contact time, but they noticeably differ in the last-contact time. Most of this difference can be attributed to the probe deformation. The probe bends after the contact with the bubble, and thus the probe sensitive tip is displaced outwards the bubble. Function $\psi_g$ was evaluated with respect to the probe initial position. If it is reevaluated by taking in account the final probe position instead, the last-contact time $t_{g2}$ occurs sooner (it is indicated by an arrow in Fig. 8b and c) and it corresponds well to $t_{op2}$. From these observations, we can draw two conclusions: (i) The rigidity of the optical probe tip is of concern for proper measurements in bubbly flows and it affects the dwell time measured near the equator. (ii) If the probe deformation is taken in account, the phase-indicator function $\psi_g$ corresponds well to $\psi_{op}$. This suggests that $\psi_{op}$ indicates correctly which phase is present at the probe tip. Finally, we remark that the shortness of time, which the probe needs to return to its initial position (of order of 1.5 ms, Fig. 6d), suggests that only the protruding glass part of the optical fiber deforms.

It is obvious that the imperfections of the optical probe (intrusiveness and deformability) introduce an error on the determination of the last-contact time $t_2$ and thus also on determination of the bubble dwell time $\tau$. In Fig. 9, the dwell times determined from the three phase-indicating functions are compared for bubbles of several sizes and in different liquids. The dwell time is plotted in a dimensionless form, $T = \tau u_1/(a_{z1} + a_{z2})$, against dimensionless bubble-probe offset, $X = x/a_x$. The dimensionless dwell time $T_{ref}$, obtained from the reference phase-indicator function $\psi_{ref}$, follows well the relationship

$$T = \sqrt{1 - X^2}, \tag{4}$$

which is expected from geometrical considerations about the observed ellipsoidal bubble shape (Fig. 2). This agreement supports our usage of $\psi_{ref}$ as a reference for quantifying the error of the optical probe measurement. The strongest deviation between $\psi_{ref}$ and Eq. (4) is found in the case of the largest bubble in water (Fig. 9c),

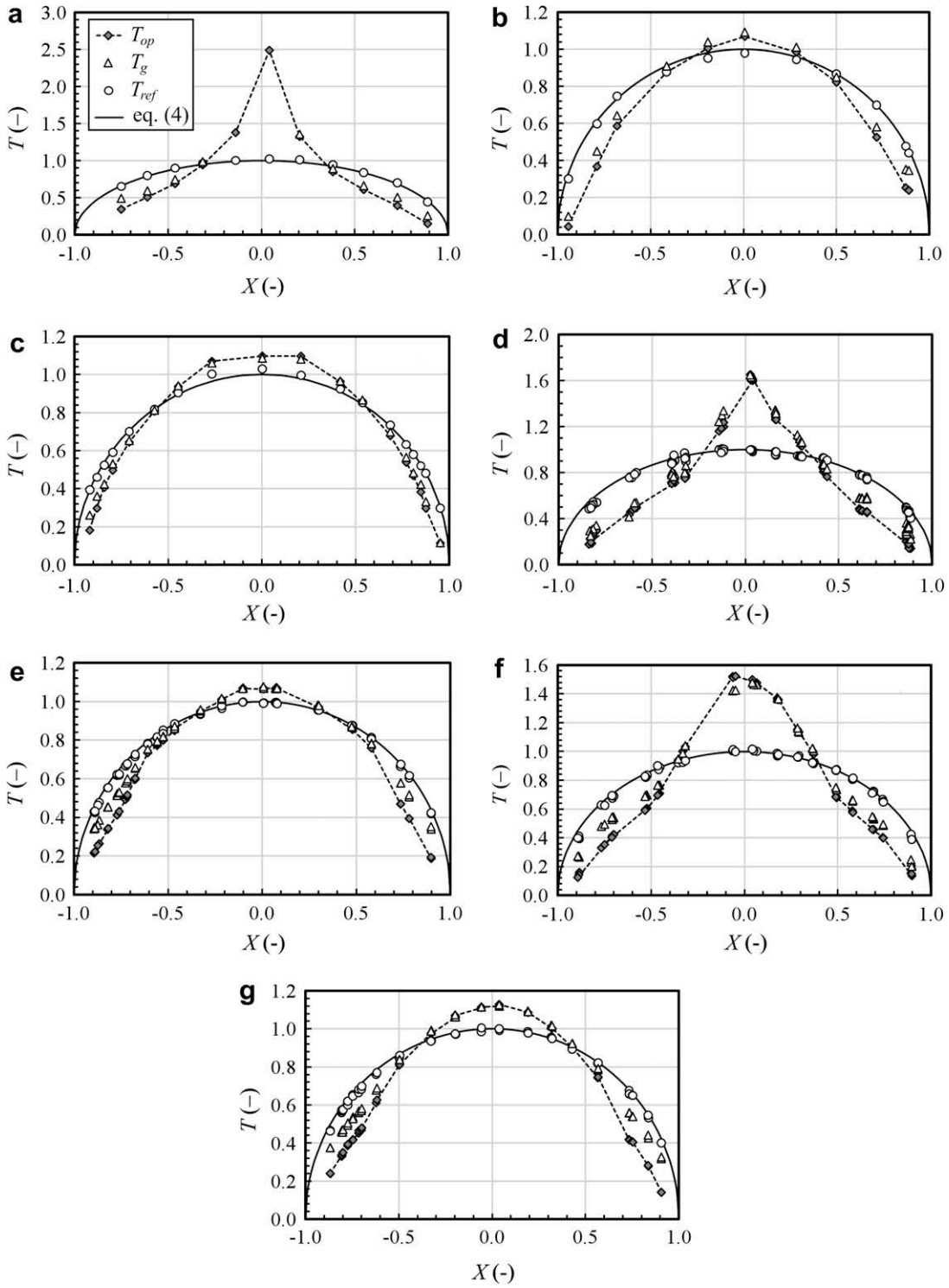


**Fig. 9.** Comparison of dimensionless dwell times $T_{op}$, $T_g$, $T_{ref}$ and Eq. (4). Experimental liquid and equivalent bubble diameter $D$ are: (a) water, 1.12 mm; (b) water, 1.48 mm; (c) water, 2.23 mm; (d) glycerin 8, 1.45 mm; (e) glycerin 8, 3.01 mm; (f) glycerin 20, 1.84 mm; (g), glycerin 20, 2.80 mm. (a–c) correspond to the first, second and fourth row in Fig 7, respectively.

and it is caused by a slight wobbling of this bubble. It is reminded that the concept of $\psi_{ref}$ is not meaningful for bubbles with unsteady shape and the case shown in Fig. 9c is considered being at the limit of usability of $\psi_{ref}$ as a reference.

Fig. 9a–c show the profiles of dwell time across the bubble for three different bubble sizes in water. Both $\tau_{op}$ and $\tau_g$ substantially differ from the ideal dwell time profile $\tau_{ref}$ for bubble sizes 1.12 mm (Fig. 9a) and smaller. An important overestimation of dwell time near bubble pole is evident. An inspection of high-speed movies shows that at zero bubble-probe offset, the bubble stops at the probe tip (Fig. 6c). For sub-millimeter bubble sizes, even a bubble rebound downward from the tip is observed. With increasing bubble size, $\tau_{op}$ and $\tau_g$ approach to $\tau_{ref}$, but some deviations are always observed (Fig. 9b and c). Coherently with the previous obser-

vations, $\tau_{op}$ and $\tau_g$ overestimates the dwell time when piercing the bubble near its pole ($X \sim 0$) and underestimates it near the equator ($X \sim -1$ or +1). The range of offsets, for which the dwell time is overestimated, is slightly growing with increasing bubble size. This effect is probably related with an increase of the bubble aspect ratio $\chi$.

Fig. 9d–g also shows the dwell time profiles, but obtained in glycerin solutions. Behavior is similar to that identified for water, except that bubbles of bigger size are now needed to get a $\tau_{op}$, which approaches to $\tau_{ref}$. This difference is related to the change in the bubble rise velocity. The difference between $\tau_{op}$ and $\tau_g$ is more pronounced in glycerin solutions than in water. The error due to probe deformation is hence more important in glycerin solutions. It is perhaps a consequence of longer dwell time, yielding to stronger impulse of forces bending the probe.

### 3.3. Change of bubble velocity

At this point, it is useful to identify a dimensionless complex, which characterizes how much the bubble is perturbed by the probe. For this purpose, we will consider the equation of bubble motion and using it, the change of bubble velocity will be estimated. Only the case of on-axis piercing ($X = 0$) is considered now.

The bubble motion equation writes as a balance of buoyancy, drag, history and added-mass forces. When the bubble enters into contact with the probe tip, a supplementary *contact force* appears and decelerates the bubble. Let us assume that the bubble is large and that its deceleration and hence the change of velocity are small. The buoyancy and drag can be then neglected, because they cancel each other. The history force can also be neglected, owing to high Reynolds number and small acceleration. The history force points upward and neglecting it thus tends to an overestimation of the bubble deceleration. The same holds for the buoyancy decreased by the drag. The remaining balance consists only of the added-mass force and the contact force. The added-mass force, which represents the inertial force of the liquid set in motion by the bubble, is

$$F_m = -\rho V \frac{d}{dt}(Cu), \tag{5}$$

where $V$ is the bubble volume, $u$ is the bubble velocity and $C$ is the added-mass coefficient (see Brennen, 1982; Magnaudet and Eames, 2000, or Simcik et al., 2008, for discussion on the added-mass force). To estimate the contact force, we assume a bubble shape with a meniscus and a wetting liquid film terminated by a three-phase line at the probe tip (Fig. 10). The three-phase line requires the surface tension to be included in the force balance. The contact force is estimated to scale with $-\pi\sigma D_{op}$ and we can hence write for it

$$F_c = -\beta \cdot \pi\sigma D_{op}, \tag{6}$$

where $\beta$ is a coefficient of the scaling and it is expected to be close to unity. The force balance $F_m + F_c = 0$ then yields for bubble deceleration

$$\frac{du}{dt} = -\frac{u_1^2}{D}\left(\frac{6\beta}{CM} + \frac{u}{u_1 C}\cdot\frac{D}{u_1}\frac{dC}{dt}\right), \tag{7}$$

where $M = (\rho D^2 u_1^2)/(\sigma D_{op})$ is the modified Weber number. The factor $u_1^2/D$ in front of brackets is an acceleration scale, the first term in brackets is a dimensionless bubble deceleration due to the contact force, and the second term in brackets is the dimensionless bubble deceleration due to a change of $C$. We will neglect this latter term. This is reasonable for the zero bubble-probe offset ($X = 0$) because the bubble frontal area does not change significantly (observe first column in Fig. 7) and thus $C$ remains unaltered. Omitting this term is not justified, however, if the probe pierces the bubble near its equator.

The period of time, during which the bubble decelerates, is of order of the dwell time and thus it scales as $(a_{z1} + a_{z2})/u_1$. Geometrical considerations yield $a_{z1} + a_{z2} = \chi^{-2/3} D$. The bubble velocity at last-contact time is therefore estimated

$$u_2 = u_1\left(1 - \frac{6\beta}{\chi^{2/3} CM}\right). \tag{8}$$

Finally, we can estimate how the dwell time $\tau_{op}$ differs from $\tau_{ref}$. The bubble has to travel over distance $a_{z1} + a_{z2}$ between the first and the last contact. The bubble velocity is decreasing from $u_1$ to $u_2$, and the time needed to travel this distance becomes longer. The average velocity is $\frac{1}{2}(u_1 + u_2)$ and assuming $\tau_{ref} = (a_{z1} + a_{z2})/u_1$ then yields for the dwell time

$$\tau_{op} = \tau_{ref}\left(1 - \frac{3\beta}{\chi^{2/3} CM}\right)^{-1} = \frac{a_{z1} + a_{z2}}{u_1}\left(1 - \frac{3\beta}{\chi^{2/3} CM}\right)^{-1}. \tag{9}$$

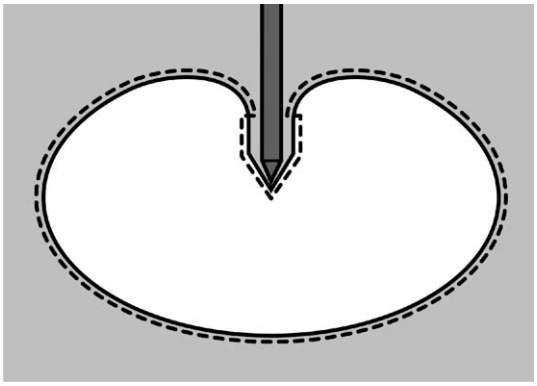

**Fig. 10.** Control volume for momentum balance of a bubble, which is in contact with the optical probe. Solid line – assumed bubble boundary, dashed line – control volume for momentum balance.

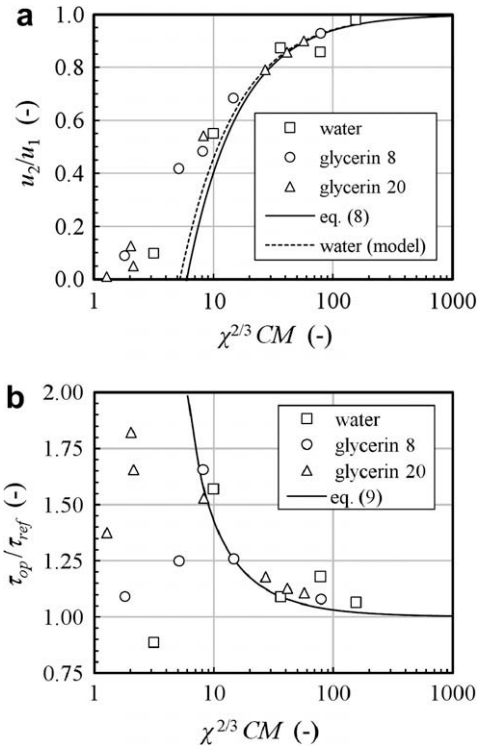


**Fig. 11.** Change of (a) bubble velocity and (b) dwell time during the bubble-probe interaction at zero bubble-probe offset, $X = 0$.

We remind that the estimations leading to Eqs. (8) and (9) assumed zero bubble-probe offset.

We will compare the prediction (8) and (9) with experimental data. We assume $\beta = 1$, which is expected if the film deposited on the probe is thin and the apparent contact angle is small. Fig. 11a compares the estimation (8) with the experimental data. The velocities $u_1$ and $u_2$ were determined from the experimental data as the $z$-component of bubble center-of-mass velocity at times $t_{ref1}$ and $t_{ref2}$, respectively. Eq. (8) correctly predicts the velocity change in the case of large and/or fast bubbles, which are characterized by $\chi^{2/3}CM > 10$. For smaller bubbles, the velocity decrease is less important than the estimate given by (8). This difference is only partly explained by neglecting the history, buoyancy and drag forces. For the case of water, we have performed a calculation of bubble motion using a model, in which the added-mass force, contact force, buoyancy, drag (following Moore 1965) and the history force (with Yang and Leal's kernel, 1991) are considered. The model details are given in Appendix A. The dependence of $u_2/u_1$ ratio on $\chi^{2/3}CM$, obtained from this model for water, is shown by a dashed line in Fig. 11a. Although it slightly approaches to the experimental data, this model still fails for $\chi^{2/3}CM < 10$.

Fig. 11b compares the experimental values of dwell time with its estimations from Eq. (9), again assuming $\beta = 1$. Again, the proposed scaling agrees well with the measurements for $\chi^{2/3}CM > 10$. In the range $\chi^{2/3}CM < 10$, which corresponds to smaller bubble size, the experimental points are widely scattered. In these cases, it is visually observed that the bubble stops its vertical motion and either rebounds from the optical probe tip, or leaves it laterally. (Observe also the downward motion of the bubble in last three frames of Fig. 6c, which corresponds to the data point for water with $\chi^{2/3}CM = 10$.) The source of data scatter may be due to a high sensitivity of bubble behavior to the bubble-probe offset in case of bubbles, which stops at the probe tip and then leaves it laterally (as shown in Fig. 6c).

It is seen that the experimental data on $u_2/u_1$ and $\tau_{op}/\tau_{ref}$, obtained in all three liquids, fall on a single curve, if plotted against $\chi^{2/3}CM$ (at least for the range $\chi^{2/3}CM > 10$). This demonstrates that the complex $\chi^{2/3}CM$ is a suitable dimensionless parameter for characterizing the bubble deceleration if the bubble-probe offset is small. Since both $\chi$ and $C$ are functions of bubble shape, which depends essentially on the Weber number, the expression $\chi^{2/3}CM$ could be replaced by $M{\cdot}f(We)$ in Fig. 11a and b. The collapse of data on a single curve suggests that the capillary number has only a minor effect on the bubble motion. It is noted that $Ca$ influences the relative importance of the history force (compared to the surface-tension force), but also the behavior of the three-phase contact line (de Gennes et al., 2004) at the probe tip and eventually the thickness of the liquid film deposit on the probe (Quéré, 1999).

According to the above reasoning, a non wetting liquid is expected to produce an opposite effect, i.e. a bubble acceleration leading to a shorter dwell time than the ideal one. It is also remarked that the Eq. (7) and hence also (8) and (9), developed for the case of still liquid, should remain valid also in the case of liquid, which flows vertically with a constant velocity. In the latter case, $u$ should be considered as an absolute bubble velocity. An experimental prove of the validity for moving liquid is missing, however.

The development of (8) and (9) and the results in Fig. 11 represented the case of zero bubble-probe offset. To complete the picture of bubble-probe interaction, Fig. 12 shows the average bubble acceleration in the vertical direction (in a dimensionless form, $A_z = (u_2 - u_1)/\tau_{ref}D/{u_1}^2$) for various bubble-probe offsets and two bubble sizes. It is reminded that these results can be biased by much larger error compared to previous results for on-axis piercing, because the bubble losses axial symmetry that is assumed in the calculation of bubble center-of-mass position, from which

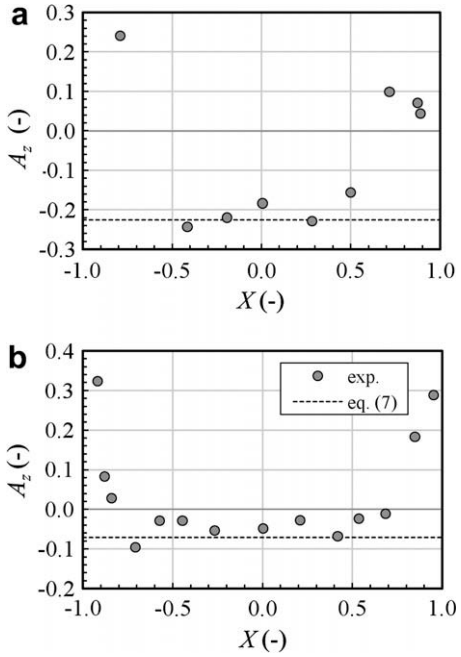


**Fig. 12.** The $z$-component of bubble mean acceleration as function of bubble-probe offset for (a) 1.48 mm bubble in water, (b) 2.23 mm bubble in water.

the velocity is deduced. Nevertheless, it is seen that the bubble deceleration is more or less constant for $|X| < 0.5$ and it roughly corresponds to the value predicted by Eq. (7), which is shown by a dashed line (the term containing $dC/dt$ in brackets of this equation was neglected). When the bubble is pierced near its equator ($|X| > 0.7$), the acceleration becomes positive, i.e. the bubble accelerates upward during the interaction. We attribute this acceleration to the bubble shrinking in the horizontal direction, which leads to a decrease of bubble frontal area and hence also of its added-mass $C$. The second term in brackets of Eq. (7) then prevails the first one and the bubble acceleration changes sign (see e.g. Lunde and Perkins, 1998, and de Vries et al., 2002, for motion of a bubble, which is changing $C$).

For a non-zero bubble-probe offset, the bubble gains also some horizontal velocity during the interaction with the probe tip. Fig. 13 shows the average bubble acceleration in the horizontal direction (again in a dimensionless form, $A_x = u_{2x}/\tau_{ref}D/{u_1}^2$, where $u_{2x}$ is the horizontal component of bubble center-of-mass velocity at time $t_{ref2}$). The remarks made on the precision of results presented in Fig. 12 apply also to this figure. Despite these reserves, the horizontal acceleration of the bubble happens to vary more or less linearly with the bubble-probe offset. The dimensionless acceleration $A_x$ is (similarly as $A_z$) decreasing with the bubble size.

### 3.4. Error on void fraction measurements

It was shown in Section 3.2 that the dwell time $\tau_{op}$ measured by the optical probe generally differs from the reference dwell time $\tau_{ref}$. In this part, we will quantify the impact of this difference on the accuracy of void fraction measurements.

Let us assume a bubbly flow, which is composed of bubbles of the same size and shape that all move with the same velocity in a direction parallel to the probe axis. The bubbles hit the optical probe at random bubble-probe offsets, as outlined in Fig. 1. Let $p_x(x)$ be the density function of the probability that a bubble will move around the probe with an offset $x$. The function $p_x(x)$ is increasing linearly with $|x|$, because of the quadratic increase of area restricted by a given radius. If only bubbles, which hit the

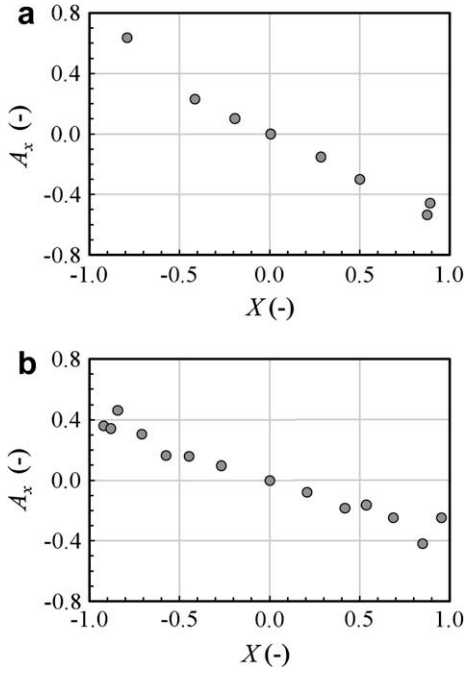


**Fig. 13.** The horizontal component of bubble mean acceleration as function of bubble–probe offset for (a) 1.48 mm bubble in water, (b) 2.23 mm bubble in water.

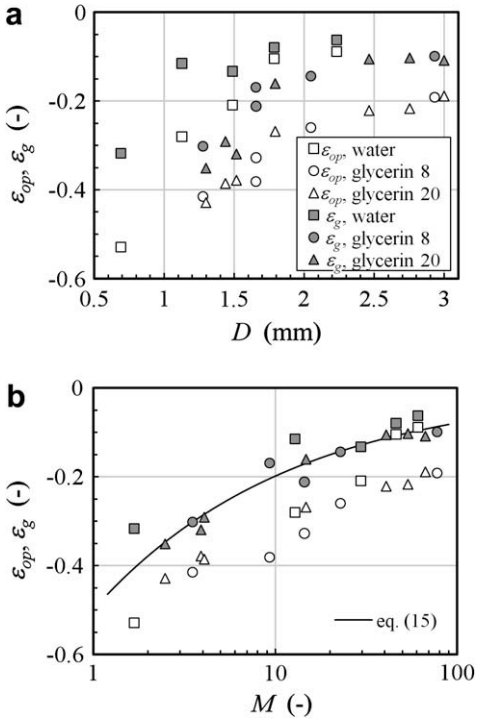


**Fig. 14.** Error on voidage measurements.

probe, are selected from an ensemble of all bubbles in the flow of interest, it is found

$$p_x(x) = \begin{cases} 2x/a_x^2 & \text{for } x \leqslant a_x, \\ 0 & \text{otherwise.} \end{cases} \tag{10}$$

(we consider only $x \geqslant 0$ in this equation, as it is a radius). It holds for the mean value of the dwell time

$$\overline{\tau} = \int_0^\infty p_x(x)\tau(x)dx = \frac{a_{z1}+a_{z2}}{u_1}\int_{-1}^{1}|X|T(X)dX. \tag{11}$$

The dimensionless dwell time $T_{ref}$ agrees reasonably with Eq. (4), see Fig. 9. We will therefore consider that it holds for the mean dwell time $\overline{\tau_{ref}}$ found by the reference probe

$$\overline{\tau_{ref}} \approx \frac{a_{z1}+a_{z2}}{u_1}\int_{-1}^{1}|X|\sqrt{1-X^2}dX = \frac{2}{3}\cdot\frac{a_{z1}+a_{z2}}{u_1}. \tag{12}$$

If the mean dwell time (or void fraction) determined by the optical probe is compared with the reference probe, it is obtained for its relative error

$$\varepsilon_{op} = \frac{\overline{\tau_{op}}}{\overline{\tau_{ref}}} - 1 = \frac{\alpha_{op}}{\alpha_{ref}} - 1 = \frac{3}{2}\int_{-1}^{1}|X|T_{op}(X)dX - 1, \tag{13}$$

and similarly for the rigid probe

$$\varepsilon_g = \frac{\overline{\tau_g}}{\overline{\tau_{ref}}} - 1 = \frac{\alpha_g}{\alpha_{ref}} - 1 = \frac{3}{2}\int_{-1}^{1}|X|T_g(X)dX - 1. \tag{14}$$

Errors $\varepsilon_{op}$ and $\varepsilon_g$ of void fraction measurements can hence be obtained by the integration of the dimensionless dwell time profiles $T(X)$. Results, obtained by a trapezoidal rule and plotted against either $D$ or $M$, are shown in Fig. 14. Both errors are always negative, i.e. the probe is underestimating the void fraction. This is linked to the factor $|X|$ in the integrand in (14), due to which the dwell times measured at large offset contribute more to the mean dwell time. The underestimation at large $|X|$ therefore is more important than the overestimation at small $|X|$ (at least for the measurements of local void fraction).

For the same bubble size and working fluid, the error $\varepsilon_g$ of the rigid probe is always smaller than that of optical probe, $\varepsilon_{op}$. It was demonstrated that the difference between corresponding phase-indicator functions, $\psi_g$ and $\psi_{op}$, is essentially due to probe deformation. The error of the void fraction measurements $\varepsilon_{op}$ thus can be divided into two parts: in (i) the error due to probe intrusive nature, $\varepsilon_g$, and (ii) the error due to probe deformability, $\varepsilon_{op}$–$\varepsilon_g$.

The error $\varepsilon_g$ is expected to depend on the three dimensionless numbers describing the bubble-probe interaction, $M$, $We$ and $Ca$. Due to the limited amount of data for $\varepsilon_g$ and their experimental scatter, we are not able to fully estimate this dependence. If $\varepsilon_g$ is plotted against $M$ only, the results more or less approach a single curve, Fig. 14b. The error $\varepsilon_g$ is controlled mostly by the bubble deformation when the probe pierces it near the equator. The collapse of data to a single curve suggests that $M$ is also a relevant parameter for describing this deformation process. If the deformation is controlled essentially by capillarity and inertia, the role of $M$ is explained in this way: The bubble shrinking leads to a horizontal displacement of a body of fluid adjacent to the bubble by a distance $\Delta x$. The relevant mass scales as $\sim\rho D^3$, the force accelerating this fluid body scales as $\sim\sigma D_{op}$ and the time available for the acceleration is $\sim D/u_1$. If we search for $\Delta x$, we obtain $\Delta x/D \sim M^{-1}$.

The experimental data on $\varepsilon_g$ are reasonably well fitted by

$$\varepsilon_g = -0.5M^{-0.4} \tag{15}$$

and this relationship (also shown in Fig. 14b) may be used for correcting the void fraction measured by the optical probe. This fit is only empirical and it should not be used outside the range of parameters considered in this study (see Table 2). Yet, the above correction is in agreement with the average errors reported in the literature. In particular, for millimeter bubbles in water, whose absolute velocities with respect to the probe were in the range 0.4–1.2 m/s, Barrau et al. (1999) report errors on void fraction ranging from −0.01 (for low velocities) to −0.15 (for large velocities). These magnitudes are consistent with Eq. (15).

It should be also underlined that the way of determining the error $\varepsilon_g$ assumes random offset of arriving bubbles, described by the probability density function $p(x)$ in form (10). In some flows conditions, the bubble positions cannot be considered as random (e.g. near walls or spargers) and the correction (15) is then not applicable.

The error due to probe deformability $\varepsilon_{op}$–$\varepsilon_g$ should depend on the probe elasticity and inertia. These probe features introduce additional dimensionless numbers required for problem description. As these features were not studied in the present work, any effort to correlate $\varepsilon_{op}$ on basis of present data is worthless.

Finally, we remark that the application of correction (15) requires that the modified Weber number $M$ is known a priori, which might not be the case in practical situations. In the case of a monodispersed bubbly flow and a sufficiently rigid probe ($\tau_{op} \approx \tau_g$), $M$ can be estimated by comparing the maximum measured dwell time with the mean dwell time. The maximum measured dwell time $\tau_{op,\max}$ corresponds to the case of zero-offset piercing, for which (9) holds. The mean dwell time $\overline{\tau_{op}}$ is correlated against $M$ (in form of an error) by (14) and (15). The comparison of both times yields

$$\frac{\overline{\tau_{op}}}{\tau_{op,\max}} = \frac{2}{3}\left(1 - \frac{3}{\chi^{2/3} C M}\right)(1 - 0.5M^{-0.4}). \tag{16}$$

Both parameters at the left-hand side of this equation can be evaluated experimentally. If $\chi$ and $C$ are known or guessed, $M$ can be estimated by solving the last equation.

### 3.5. Error on the dwell time p.d.f.

In the previous section, the consequences of the probe intrusive nature on the mean dwell time were investigated. However, the interaction between the bubble and the probe modifies also the dwell time distribution. The expected impact on the dwell time p.d.f. is examined in this section.

Again, let us assume a bubbly flow composed of bubbles of the same size and shape, which all move with the same velocity in a direction parallel to the optical probe axis. The bubbles hit the probe with a random offset whose p.d.f. $p_x(x)$ is given by Eq. (10). Because the dwell time $\tau$ depends on $x$, $\tau$ also is a random variable. It holds for its p.d.f. $p_\tau(\tau)$

$$p_\tau(\tau) = -p_x(x(\tau))\frac{dx(\tau)}{d\tau} = -\frac{2x(\tau)}{a_x^2}\frac{dx(\tau)}{d\tau} \tag{17}$$

where the dependence $x(\tau)$ expresses the offset $x$, at which the dwell time $\tau$ is measured, and it represents the inverse function of $\tau(x)$, which was shown (in a dimensionless form) in Fig. 9. The minus sign appears in (17) because $x(\tau)$ is a monotonically decreasing function (we limit here to $x \geqslant 0$). The ideal dependence between $x$ and $\tau$ follows the behavior given by Eq. (4) and the ideal dwell time p.d.f. then is

$$p_\tau(\tau) = \begin{cases} \frac{2\tau u_1^2}{(a_{z1}+a_{z2})^2} & \text{for } \tau \leqslant \frac{a_{z1}+a_{z2}}{u_1}, \\ 0 & \text{otherwise.} \end{cases} \tag{18}$$

This is a standard result, which has been derived many times (e.g. Cartellier and Achard 1991 and references therein), but which is almost never observed in practice.

An example of a practically observed dwell time p.d.f. is shown in Fig. 15. The solid line represents the dwell time p.d.f. (in a dimensionless form, $T = \tau u_1/(a_{z1} + a_{z2})$, $p_T = (a_{z1} + a_{z2})/u_1 \cdot p_\tau$), which has been measured by Andreotti (2009). In his experiment, an almost mono-dispersed bubbly flow was produced by an array of 289 capillary tubes (with inner diameter 90 μm and 20 mm long) in an air-lift loop similar to that used by Cartellier and Rivière (2001). Hence differently to our experiments reported above, the liquid was not stagnant in Andreotti's experiment, but it was flowing upward. The working liquid was a glycerin solution (with density ranging from 1120 to 1160 kg m$^{-3}$ and kinematic viscosity from $6 \times 10^{-6}$ to $8 \times 10^{-6}$ m$^2$ s$^{-1}$). Bubbles were spherical and the standard deviation of their size was less than 5.5% of the mean size. The bubble rise velocity (relative to the liquid) was 10 cm/s. The dwell time was measured using an optical probe of similar design as that one used in this study, but with 100 μm diameter. The dwell-time p.d.f. was measured for two different operating conditions. The corresponding gas hold-ups, bubble sizes, bubble absolute velocities ($u_1$) and mean liquid velocities ($u_L$) are given in Table 3. This table provides also the values of modified Weber number, which is based on bubble absolute velocity.

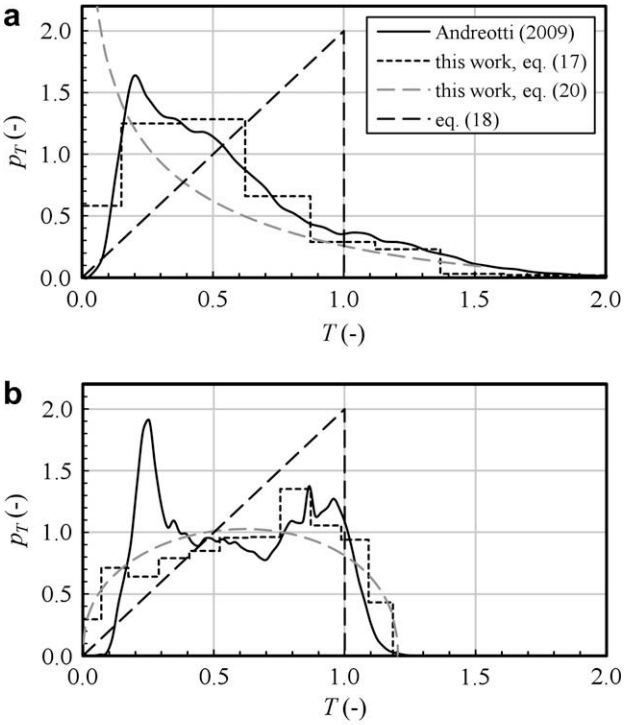


**Fig. 15.** Comparison of the dwell time p.d.f. data (provided by Andreotti (2009)) to its estimates based on present experiments. The modified Weber number for Andreotti's data and for the present experiment are (a) $M = 13.2$ and 12.6, respectively, and (b) $M = 48.8$ and 45.9, respectively.

As it is seen from Fig. 15, the observed dwell-time p.d.f. considerably differs from the ideal distribution given by (18), which is also shown. In the case of smaller $M$ (Fig. 15a), $p_\tau(\tau)$ even has an inverse character with the highest probability for the short dwell times. The deviation of observed dwell time p.d.f. from an ideal distribution is explained by the difference between the measured dwell time $\tau_{op}$ and its ideal counterpart $\tau$. Fig. 15 shows by dotted line the dwell time p.d.f., which was obtained using Eq. (17) on the basis of the dwell time $\tau_{op}$ profiles measured in this work. The cases with similar value of $M$ were chosen for comparison and the corresponding bubble parameters are also provided in Table 3. A relatively good agreement is observed between the $p_\tau(\tau)$ measured by Andreotti (2009) and that obtained by Eq. (17) from the present data. Both p.d.f. differ mostly in the probability of short dwell times. Results obtained by (17) for short dwell times are indeed susceptible to large errors, because the derivative $dx(\tau)/d\tau$ cannot be precisely evaluated for piercing near the bubble equator (note the insufficient number of experimental points for evaluating the $\tau(x)$ dependence near the equator, Fig. 9, that combines with the distorted response of the probe at large eccentricities).

**Table 3**
Operating conditions of Andreotti's (2009) experiments and of cases of present experiment chosen for comparison.

| Corresponding figure | 15a | 15b |
|---|---|---|
| *Andreotti's (2009) experiments* | | |
| $\alpha$ (%) | 7.27 | 2.4 |
| $D$ (mm) | 1.60 | 1.58 |
| $u_1$ (cm/s) | 19 | 37 |
| $u_L$ (cm/s) | 9 | 27 |
| $M$ (−) | 13.2 | 48.8 |
| *Present experiments, cases chosen for comparison with Andreotti's data* | | |
| Working liquid | Water | Water |
| $D$ (mm) | 1.12 | 1.78 |
| $u_1$ (cm/s) | 30.6 | 36.6 |
| $u_L$ (cm/s) | 0 | 0 |
| $M$ (−) | 12.6 | 45.9 |
| $k_{op}$ (−) | 2.51 | 0.69 |
| $n_{op}$ (−) | 1.20 | 1.40 |

The calculation of dwell time p.d.f. from the experimental $\tau_{op}(x)$ profiles using (17) is technically tricky because of the differentiation of scarce experimental data. To explain the inverse character of the dwell time profile, we fit therefore the experimental $T(X)$ profile with an empiric relation

$$T = k(1 - X^n)^{1/n}, \tag{19}$$

where $k$ and $n$ are the adjustable parameters. Fig. 16b shows the exponent $n_g$ found by fitting the $T_g$ profiles (Fig. 9). The value of $n_g$ increases with $M$ and its value ranges from 0.9 to 1.56. Similar values of the exponent are obtained by fitting the $T_{op}$ profiles, which ranges from 0.65 to 1.43; we do not show results on $n_{op}$ here, because the fit (19) is less suitable for $T_{op}$ profiles. However, both $n_g$ and $n_{op}$ are significantly smaller than its ideal value ($n = 2$), for which the fit (19) recovers the ideal dwell time profile, Eq. (4).

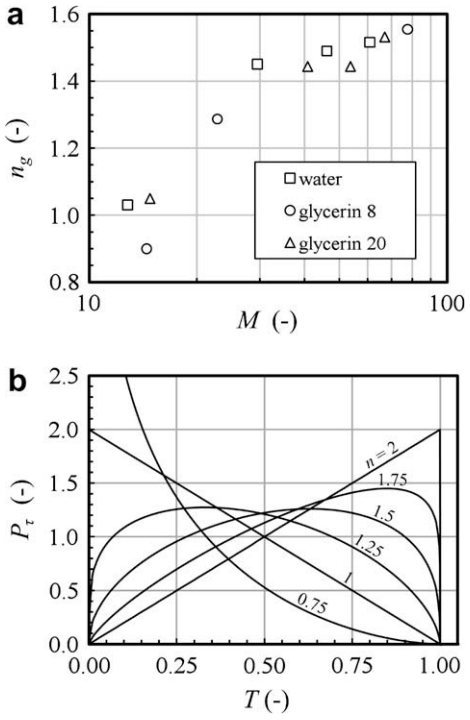


**Fig. 16.** (a) Exponent $n_g$ found by fitting $T_g(X)$ profiles by Eq. (19). (b) Dwell-time p.d.f. predicted by Eq. (20) for several values of $n$, assuming $k = 1$.

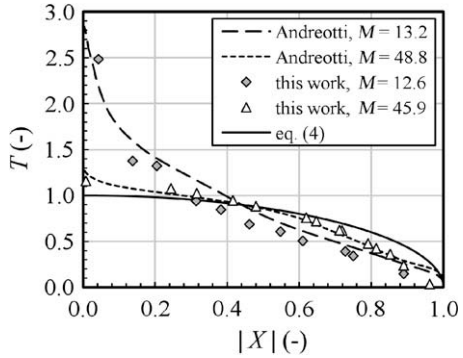


**Fig. 17.** Dwell time profile obtained from Andreotti's (2009) dwell time p.d.f. using Eq. (21) and its comparison with $T_{op}$ profiles of this work.

Substituting the empirical fit (19) into (17) yields the expected dwell time p.d.f., which is in form

$$p_\tau(\tau) = \begin{cases} \frac{2}{\tau}\left(\frac{\tau u_1}{k(a_{z1}+a_{z2})}\right)^n \left[1 - \left(\frac{\tau u_1}{k(a_{z1}+a_{z2})}\right)^n\right]^{\frac{2}{n}-1} & \text{for } \tau \leqslant k\frac{a_{z1}+a_{z2}}{u_1}, \\ 0 & \text{otherwise.} \end{cases} \tag{20}$$

The coefficient $k$ stretches the $p_\tau(\tau)$ distribution, while its shape is given essentially by the exponent $n$. Examples of $p_\tau(\tau)$ estimated by (20) are shown in Fig. 16b for several values of $n$ and for $k = 1$. Assuming $n = 2$, the dwell-time p.d.f. reduces to (18). We see, however, that the peak in $p_\tau(\tau)$ moves toward shorter dwell times if the exponent $n$ decreases. The dwell time p.d.f. gets completely inverted for $n = 1$. Finally, Fig. 15 also compares the dwell time p.d.f., which were obtained using Eq. (20) by fitting the corresponding dwell time profiles $T_{op}(X)$, to the Andreotti's results and also to the p.d.f. obtained using (17) (values of $k_{op}$ and $n_{op}$, used for the fit, are given in Table 3). A reasonable agreement is observed especially in the case of higher $M$, Fig. 15b.

The relationship (17) between the dependence $x(\tau)$ and the dwell-time p.d.f. $p_\tau(\tau)$ can also be used inversely: if $p_\tau(\tau)$ is measured experimentally in a flow with mono-dispersed randomly distributed bubbles, the $\tau = \tau(x)$ profile can be deduced. The dependence $x(\tau)$ is found by substituting (10) in (17) and integrating. One easily obtains

$$\left(\frac{x(\tau)}{a_x}\right)^2 = 1 - \int_0^\tau p_\tau(\tau)d\tau. \tag{21}$$

and $\tau(x)$ is then the inverse function of $x(\tau)$. Fig. 17 shows the dwell time profiles, obtained from the Andreotti's data (Fig. 15) in this way, and compares them with the $T_{op}(X)$ profiles found in this work for bubbles with similar values of modified Weber number $M$. Taking in account the different bubble shape, difference in liquid velocity and also different probe size, results on the dwell time profile for the same $M$ are similar. A relatively good agreement of data based on Andreotti's experiment with results of this work (Figs. 15 and 17) demonstrates the suitability of $M$ for the description of the probe intrusive nature. It also demonstrates that results of this work can be applied (at least to some extent) also to the case of moving liquid.

The $\tau(x)$ profile, obtained using Eq. (21) from the dwell time p.d.f. measured in a mono-dispersed bubbly flow, can be used for determination of the local void fraction error using Eq. (13) in the same manner as the $\tau(x)$ profiles received in present experiments.

## 4. Concluding remarks

We have investigated the impact of the intrusive nature of a mono-fiber optical probe on the measurement accuracy of some

bubbly flows characteristics. This sensor significantly alters the behavior of bubbles when they come into contact with the solid probe. Bubbles pierced near their pole decelerate, and the probe detects dwell times longer than it should. An opposite effect is observed for bubbles pierced near their equator: as the bubbles shrink horizontally, the probe tip leaves the bubble sooner compared to an unperturbed bubble, and it indicates shorter dwell time. For near-equator piercing, the error can be further increased by the probe deformability: indeed, bubbles are able to displace the sensitive tip outward and the indicated dwell times are further shortened.

These observations have important consequences for the use of optical probes. First, because of the deceleration experienced by the bubble at zero offset, the maximum detected gas dwell time gets longer. The maximum detected gas dwell time should hence not be used as such to infer the maximum chord length through bubbles except if the deceleration at impact becomes weak enough. The conditions for which this condition is fulfilled have been investigated in Section 3.3.

Second, the mean gas dwell time does not provide the actual mean chord length except at large modified Weber numbers. As a result, the local void fraction indicated by the probe is smaller than it would be if observed by a non-intrusive method, as shown in Section 3.4. In the range of parameters covered in this study, the error on the local void fraction measured by a rigid probe can be corrected using Eq. (15). This correction requires the modified Weber number to be known. It can be estimated by comparing the maximum and mean dwell time (Eq. (16)). The correction is applicable, however, only to a mono-dispersed bubbly flow. It can always be used a posteriori to evaluate the typical measurement uncertainty, anyway.

Third, the dependence of the dwell time error on the piercing location leads to an important change of the measured dwell time p.d.f. Consequently, deducing the bubble size distribution by inverting a formula, which relates the chord p.d.f. to the size p.d.f. (Cartellier 1999), might lead to erroneous results, if the ideal probe behavior is assumed. Present experiments also explain reasons, for which the dwell time p.d.f.'s observed in practice strongly differ from the ideal distribution.

This investigation has provided some necessary conditions under which the raw data collected from an optical probe can be used with confidence. These conditions are also helpful to select a probe adapted to a given application. The key parameter is the modified Weber number, which characterizes the bubble ability to overcome surface-tension forces arising from the contact with the probe tip. From our experiments, the modified Weber number above 50 seems to ensure an uncertainty less than 10% on both the local void fraction and on the maximum chord length. At the same time, the rigidity of the optical probe tip should be sufficient to limit its deformation.

This investigation has also provided a procedure to correct both the void fraction and the mean chord measurements in flows with mono-dispersed ellipsoidal bubbles. The dependence of the dwell time on the bubble-probe offset can be calculated from the dwell time p.d.f. using Eq. (21) and the error is then obtained by (13). Although of limited range of applicability, we believe that this procedure can be useful in many practical situations, at least to provide the order of magnitude of the measurement uncertainty. It could be useful for systematic quantification of the measurement uncertainties associated with various types of probes.

Our investigation was carried out only in stagnant liquid and for a single probe size. Our data, however, agrees with that obtained by Andreotti (2009) in his experiments with smaller probe and in flowing liquid. This agreement suggests that the proposed scaling is correct and that it can be (at least to some extent) applied also to the case of moving liquid. These conclusions deserve to be further confirmed, anyway, and they should hence be used with a care. Finally, we have demonstrated that the probe deformability might play an important role in the measurement uncertainty, but a quantitative study of this feature is also a due.

An unambiguous interpretation of the detected dwell time into a form of bubble size distribution whatever the flow regime remains a formidable task. Yet, the proposed methodology to relate the bubble-probe offset and measured gas dwell time opens the way to a systematic quantification of the intrusive nature of local detection probes, and thus to more reliable measurements using these sensors.

## Acknowledgements

Authors express gratitude to Marcelo Andreotti for providing us data shown in Fig. 15. A review of the manuscript by Jaroslav Tihon and Maria Zednikova is greatly appreciated. The research was supported by GA AV under Project No. IAA 200720801; under this project, the ICPF team has focused especially in the Section 3.3 dealing with the forces acting on the bubbles. Indispensible equipment (the optical probe, high-speed camera, optical equipment and data acquisition system) was acquired in the past for projects supported by Grant Agency of the Czech Republic (Project Nos. 104/07/1110 and 104/06/P287).

## Appendix A

In this appendix, we describe the model, by which the dashed line in Fig. 11a is calculated. The model considers a bubble, which rises steadily at its terminal velocity and which comes suddenly (at time $t_1$) into contact with the tip of optical probe. After $t_1$, the motion is modeled by balancing the added-mass force, contact force, buoyancy force, drag force and history force. Only the rectilinear motion in the vertical direction is considered. All forces and also the velocity are hence expressed here as scalars, which are positive if the corresponding vectors point upward.

The terminal rise velocity and aspect ratio (before $t_1$) are calculated by balancing the buoyancy and drag forces,

$$F_b + F_D = 0. \tag{22}$$

The buoyancy and drag forces are expressed in common way

$$F_b = \rho g V, \tag{23}$$

$$F_D = -\frac{\pi}{8} C_D D^2 \rho u |u|. \tag{24}$$

Moore's (1965) solution for the drag is used, thus the drag coefficient is calculated as

$$C_D = \frac{48 G(\chi)}{Re}[1 + H(\chi) \cdot Re^{-1/2}]. \tag{25}$$

For functions $G(\chi)$ and $H(\chi)$, see Eq. (2.12) and Table 1, respectively, of Moore's (1965) article. The Reynolds number is defined in standard way, $Re = \rho D|u|/\mu$. The bubble aspect ratio $\chi$ is also obtained by Moore's (1965) prediction

$$We = 4\chi^{-4/3}(\chi^3 + \chi - 2)\left(\chi^2 \sec^{-1}\chi - \sqrt{\chi^2 - 1}\right)^2 (\chi^2 - 1)^3 \tag{26}$$

the Weber number is also in standard form, $We = \rho D u^2/\sigma$. The last equation defines function $\chi = \chi(We)$ in an implicit form. Eqs. (22)–(26) are solved iteratively, yielding the rise velocity and the aspect ratio before the first contact with the probe; these values are denoted $u_1$ and $\chi_1$, respectively.

At time $t_1$, the bubble comes into contact with the optical probe. Its velocity starts to evolve in time from the initial value $u_1$ (the initial condition is hence $u(t_1) = u_1$). We assume that the aspect ratio

remains unchanged even after the contact, $\chi = \chi_1$. The evolution of bubble velocity is calculated by balancing all forces,

$$F_m + F_c + F_b + F_D + F_h = 0. \quad (27)$$

The expression for the added-mass force, $F_m$, is given by Eq. (5). The added-mass coefficient $C$ is calculated using (2) and (3) and because of the assumption of unchanging $\chi$, $C$ is also constant. The contact force, $F_c$, is given by (6), and we consider $\beta = 1$. Eq. (23) holds for buoyancy, and the drag is calculated using (24) and (25). Finally, the history force is estimated by Yang and Leal's (1991) expression

$$F_h(t) = -4\pi\mu D \int_{-\infty}^{t} \exp\left(\frac{36\mu(t-t_p)}{\rho D^2}\right) \mathrm{erfc}\left(\sqrt{\frac{36\mu(t-t_p)}{\rho D^2}}\right) \frac{du(t_p)}{dt_p} dt_p. \quad (28)$$

Yang and Leal's (1991) solution is valid for spherical bubbles only, but to our knowledge, there is no solution available for the case of oblate bubbles. When calculating the history force, the past accelerations of the bubble are integrated. Consistently with assumption of steady rise before $t_1$, $du(t_p)/dt_p$ is zero for $t_p < t_1$.

An integro-differential equation for the bubble velocity $u(t)$ is obtained by substituting expressions for forces into (27). A term containing the first derivative of velocity appears in this equation due to the form of the added-mass force, and a term with the integral of past accelerations appears due to the history force. The resulting equation is solved numerically using a simple first-order discretization.

When calculating the last-contact velocity $u_2$, which is shown by dashed line in Fig. 11a, we proceed in the following way: for a given bubble size, we calculate the terminal rise conditions, i.e. $u_1$ and $\chi_1$. Corresponding values of $C$ and $M$ are calculated. The evolution of velocity $u(t)$ after the first contact is obtained by solving the system of Eqs. (27), (5), (6), (23), (24), (25), and (28) together with the initial condition $u(t_1) = u_1$. The velocity is integrated to obtain the evolution of bubble position. Last-contact time $t_2$ is found as time required for displacing the bubble by $D\chi^{-2/3}$ since $t_1$, and the corresponding velocity $u_2$ is evaluated.

In this way, a single point of the dashed curve in Fig. 11a is found. All the procedure is repeated for different bubble sizes to obtain the entire curve. This calculation was carried out only for water, which was the only liquid allowing the use of the drag law (25).

## References


Andreotti, M., 2009. Ecoulements à bulles: micro-structuration et agitation induite à nombre de Reynolds particulaire modéré. Ph.D. Thesis, Institut National Polytechnique de Grenoble.

Barrau, E., Rivière, N., Poupot, C., Cartellier, A., 1999. Single and double optical probes in air-water two-phase flows: real time signal processing and sensor performance. Int. J. Multiphase Flow 25, 229–256.

Blanco, A., Magnaudet, J., 1995. The structure of the axisymmetrical high-Reynolds number flow around an ellipsoidal bubble of fixed shape. Phys. Fluids 7, 1265–1274.

Brennen, C.E., 1982. A review of added mass and fluid inertial forces. Research Report N62583-81-MR-554. Naval Civil Engineering Laboratory, Port Hueneme.

Cartellier, A., 1992. Simultaneous void fraction measurement, bubble velocity, and size estimate using a single optical probe in gas-liquid two-phase flows. Rev. Sci. Instrum. 63, 5442–5453.

Cartellier, A., 1998. Measurement of gas phase characteristics using new monofiber optical probes and real-time signal processing. Nucl. Eng. Des. 184, 393–408.

Cartellier, A., 1999. Post-treatment for phase detection probes in non-uniform two-phase flows. Int. J. Multiphase Flow 25, 201–228.

Cartellier, A., Achard, J.L., 1991. Local phase detection probes in fluid fluid 2-phase flows. Rev. Sci. Instrum. 62, 279–303.

Cartellier, A., Barrau, E., 1998a. Monofiber optical probes for gas detection and gas velocity measurements: optimised sensing tips. Int. J. Multiphase Flow 24, 1295–1315.

Cartellier, A., Barrau, E., 1998b. Monofiber optical probes for gas detection and gas velocity measurements: conical probes. Int. J. Multiphase Flow 24, 1265–1294.

Cartellier, A., Rivière, N., 2001. Bubble-induced agitation and microstructure in uniform bubbly flows at small to moderate particle Reynolds numbers. Phys. Fluids 13, 2165–2181.

Chaumat, H., Billet-Duquenne, A.-M., Augier, F., Mathieu, C., Delmas, H., 2007. On the reliability of an optical fibre probe in bubble column under industrial relevant operating conditions. Exp. Therm. Fluid Sci. 31, 495–504.

Clift, R., Grace, J., Weber, M.E., 1978. Bubbles, Drops, and Particles. Academic Press.

Duineveld, P.C., 1995. The rise velocity and shape of bubbles in pure water at high Reynolds-number. J. Fluid Mech. 292, 325–332.

de Gennes, P.-G., Brochard-Wyart, F., Quéré, D., 2004. Capillarity and Wetting Phenomena. Springer.

Grimes, C.A., Dickey, E.C., Pishko, M.V., 2006. Encyclopedia of Sensors. American Scientific Publishers, Stevenson Ranch.

Guet, S., Fortunati, S.V., Mudde, R.F., Ooms, G., 2003. Bubble velocity and size measurement with a four-point optical fiber probe. Particle Particle Syst. Char. 20, 219–230.

Harteveld, W., 2005. Bubble Columns: Structures or Stability. Ph.D. Thesis, Delft Technical University.

Julia, J.E., Harteveld, W.K., Mudde, R.F., Van den Akker, H.E.A., 2005. On the accuracy of the void fraction measurements using optical probes in bubbly flows. Rev. Sci. Instrum. 76, 035103.

Kiambi, S.L., Duquenne, A.M., Dupont, J.B., Colin, C., Risso, F., Delmas, H., 2003. Measurements of bubble characteristics: comparison between double optical probe and imaging. Can. J. Chem. Eng. 81, 764–770.

Lamb, H., 1932. Hydrodynamics. Dover Publications.

Liju, P.Y., Machane, R., Cartellier, A., 2001. Surge effect during the water exit of an axisymmetric body traveling normal to a plane interface: experiments and BEM simulations. Exp. Fluids 31, 241–248.

Lunde, K., Perkins, R.J., 1998: Shape Oscillations of Rising Bubbles. Appl. Sci. Res. 58, 387–408.

Magnaudet, J., Eames, I., 2000. The motion of high-Reynolds-mumber bubbles in inhomogeneous flows. Annu. Rev. Fluid Mech. 32, 659–708.

Miller, N., Mitchie, R.E., 1970. Measurement of local voidage in liquid/gas two-phase flow systems using a universal probe. J. Brit. Nucl. Energy Soc. 2, 94–100.

Moore, D.W., 1965. Velocity of rise of distorted gas bubbles in a liquid of small viscosity. J. Fluid Mech. 23, 749–766.

Quéré, D., 1999. Fluid coating on a fiber. Annu. Rev. Fluid Mech. 31, 347–384.

Revankar, S., Ishii, M., 1992. Local interfacial area measurement in bubbly flow. Int. J. Heat Mass Transfer 35, 913–925.

Revankar, S., Ishii, M., 1993. Theory and measurement of local interfacial area using a four sensor probe in two-phase flow. Int. J. Heat Mass Tranfer 36, 2997–3007.

Saito, T., Mudde, R.F., 2001. Performance of 4-tip optical fiber probe and bubble characterizations by the probe in turbulent bubbly flows. In: Proceedings of the 4th International Conference on Multiphase Flow (ICMF-2001). New Orleans, USA.

Simcik, M., Ruzicka, M.C., Drahos, J., 2008. Computing the added mass of dispersed particles. Chem. Eng. Sci. 63, 4580–4595.

Tropea, C., Yarin, A.L., Foss, J.F., 2007. Springer Handbook of Experimental Fluid Mechanics. Springer, Berlin.

Vejrazka, J., Fujasova, M., Stanovsky, P., Ruzicka, M.C., Drahos, J., 2008. Bubbling controlled by needle movement. Fluid Dyn. Res. 40, 521–533.

de Vries, J., Luther, S., Lohse, D., 2002. Induced bubble shape oscillations and their impact on the rise velocity. Eur. Phys. J. B 29, 503–509.

Wedin, R., Davoust, L., Cartellier, A., Byrne, P., 2003. Experiments and modelling on electrochemically generated bubbly flows. Exp. Therm. Fluid Sci. 27, 685–696.

Yang, S.M., Leal, L.G., 1991. A note on memory-integral contributions to the force on an accelerating spherical drop at low reynolds-number. Phys. Fluids A-Fluid 3, 1822–1824.